An Optimized CPML Formulation for High Order FVTD Schemes for CED

Dinshaw S. Balsara, Saurav Samantaray, Kaiser Niknam, Jamesina J. Simpson and Gino Montecinos

Abstract— **Developing an optimal perfectly matched layer (PML) formulation is crucial for efficient CED calculations. This becomes imperative for higher order CED schemes. If a PML causes spurious back-reflection of waves into the computational domain, those waves will be evolved by the higher order scheme as if they are physical. We present a PML that is conformant in its collocation and discretization with second, third and fourth order finite volume time-domain (FVTD) schemes that preserve global divergence. We present optimal PML parameters for second, third and fourth order FVTD schemes based on a careful numerically-motivated, optimization. At each order of accuracy we have to repeat the optimization study in order to get the best performance. We find that with increasing order of accuracy we can achieve greater suppression of spuriously reflected waves from the PML layer, especially at late times. Taking the finite difference time-domain (FDTD) method as a baseline, our schemes show as much as three orders of magnitude improvement in the suppression of late time reflection of waves from the PML layer. The schemes rely on several newly-invented reconstruction strategies and a very novel Implicit Taylor ADER (Arbitrary accuracy DERivatives) predictor step. Riemann solvers provide the corrector step.**

Index Terms—**Electromagnetic propagation, computational electromagnetics, FDTD, FVTD, DGTD, PML.**

I. INTRODUCTION

THE numerical solution of Maxwell's equations, also referred to as computational electrodynamics (CED), is central to numerous applications in science and engineering. For more than fifty years, the finite-difference time-domain (FDTD) method (Yee [46], Taflove and Hagness [43], Taflove, Oskooi and Johnson [42]) has been the method of choice for CED applications. The popularity of FDTD, as well as its fidelity to the physics, stems from its use of the Yee-type staggering of electric and magnetic field intensities. FDTD provides a direct interpretation of the two curl-type equations given by Faraday's and extended Ampere's laws and a natural satisfaction of the constraint equations given by Gauss' law for electric charge and the absence of magnetic monopoles. It also provides for a perfectly matched layer (PML) formulation at the boundaries of the mesh, which allows waves that are propagating towards the boundary to seamlessly propagate out of the computational domain without significant back-reflection into the computational domain (Berenger [22], [23], Katz, Thiel and Taflove [32], Taflove and Hagness [43] Gedney [24], [25], [28], Roden and Gedney [38], Gedney and Zhao [27]). The mimetic preservation of constraints, along with the computational efficiencies achieved via PML, enabled the PML-enabled FDTD scheme to play a dominant role in CED despite the fact that the method was only second order accurate. Attempts to go past second order with FDTD have not proved too successful. Towards the end of his career, A. Taflove used to speculate whether we could improve PML by treating the source terms fully implicitly while the remaining terms were treated explicitly? This paper answers that question in the affirmative.

There has been an effort to develop higher order methods for CED that are based on higher order methods for fluid mechanics (Munz et al. [37], Ismagilov [31], Barbas and Velarde [16], Cockburn and Shu [19], [20]). Such efforts have yielded an early generation of discontinuous Galerkin time-domain (DGTD) methods (Hesthaven and Warburton [30], Cockburn, Li and Shu [21], Lu, Zhang and Cai [36], Ren *et al.* [39], Wang *et al.* [45], Sun et al. [40], Angulo *et al.* [1]) which do not have the same mimetic properties as FDTD; i.e. they are not globally divergence-constraint preserving. It is possible to appreciate the crux of the problem by realizing that DG methods, like all higher order Godunov methods for fluids, are based on a zone-centered collocation of fluid variables which are updated using fluxes that are evaluated (using Riemann solvers) at the faces of the mesh. The Yee-type staggering of variables fundamentally requires a facial collocation of vector field components that are updated in a globally divergence constraint-preserving fashion using edge-collocated variables.

But there is another field of study, namely numerical magnetohydrodynamics (MHD), that also relies on a Faraday's law update for the magnetic field. For a while, it seemed like that field underwent an independent line of evolution with the development of multidimensional Riemann solvers that could be applied to the edges of the mesh (Balsara [5], [6], [7], Balsara and Nkonga [10]) and the development of globally divergence-preserving reconstruction (Balsara [2], [3], [4]) that relied on facial collocation of vector fields. The inevitable cross-fertilization of ideas happened when one of us realized these were just the right advances for obtaining a Yee-type mimetic collocation of CED variables that could indeed be extended to high order. Therefore, the stage was set for bringing insights from modern numerical MHD methods into CED. This was done for globally divergence constraint-preserving finite volume time-domain (FVTD) methods in Balsara *et al.* ([9], [11], [12]) and globally divergence constraint-preserving DGTD methods (Balsara and Käppeli [13], Hazra *et al.* [29], Balsara and Simpson [14]). The facial collocation of variables and their high order constraint-preserving reconstruction ensures that this new generation of FVTD and DGTD methods can reach high orders of accuracy.

The use of multidimensional Riemann solvers at the edges of the mesh ensures that the methods are very stable, multidimensionally upwinded and globally divergence constraint-preserving.

To retrace the plan that made FDTD a highly successful method, one has to build into these novel FVTD and DGTD schemes the same facility for handling PML boundary conditions. Since the new generation of FVTD schemes can reach very high order of accuracy, our ***first goal*** is to try and achieve optimal PML performance at all orders. While working towards this goal, we discovered that the form of the complex frequency shifted PML, a.k.a. CPML (Gedney [24], [28], Roden and Gedney [38], Chew and Jin [18], Gedney *et al*. [26], Chen *et al*. [17]), can play a big role in yielding implementations that can either be successful or unsuccessful. In other words, the structure of the equations plays an important role in the success of the PML algorithm. The physical reason is that the FVTD scheme has a particular discretization on the mesh and it is very advantageous if the CPML equations also have a conformant discretization on the mesh. Therefore, our ***second goal*** is to derive and describe a set of CPML equations that are conformant with the constraint-preserving structure of Maxwell's equations.

We also find that FVTD schemes at each specific order of accuracy have to be optimized for peak performance in a different way. Therefore, our ***third goal*** is to obtain optimal PML parameters for second, third and fourth order FVTD schemes based on a careful optimization study. In this paper, we restrict attention to optimizing PML for divergence constraint-preserving FVTD, leaving a thorough study of optimized PML for divergence constraint-preserving DGTD to a subsequent paper.

The above paragraphs have presented a big-picture approach to CED and PML. But a successful implementation of CED and PML requires a third algorithmic ingredient. While the reconstruction and the multidimensional Riemann solvers provide high order and constraint preservation respectively, there is a third feature in the CED and PML equations that also demands attention. It stems from the fact that the source terms can strongly dominate the hyperbolic PDE. Numerical implementations for hyperbolic PDEs that are not incredibly stable in the face of stiff source terms tend to become unstable. It is for this reason that Balsara *et al*. ([9], [11], [12]) paid particular attention to CED formulations that could handle stiff source terms. They presented certain ADER (Arbitrary accuracy DERivative) methods for the accurate temporal update of Maxwell's equations in the face of stiff source terms. In fairness, even Maxwell's equations with large conductivities benefit from ADER methods that are simultaneously highly accurate in their time integration and provide a fully time-implicit (and therefore very stable) treatment of source terms, as shown in Balsara *et al*. ([11], [12]). But the structure of the PML equations is such that they require an even stronger dose of stability in the face of stiff source terms. It is for this reason that a ***fourth goal*** of this paper is to present a novel Implicit Taylor form of ADER which is particularly well-suited for CED in general and PML in particular. We present such a formulation here.

PML is applied to a thin layer of zones, often 6 to 10 zones wide, at the outer boundary of the mesh. As a result, within just these zones, the PML is required to provide an almost achromatic damping of all waves that impinge on this layer from almost any direction. As a result, the structure of the PML equations, and the collocation of PML variables on the faces of the mesh, becomes very important. Section II describes the derivation of the PML equations used here; with some additional helpful material in Supplement A. Section III describes the collocation of electric and magnetic flux densities at the faces of the mesh; with some additional helpful material in Supplement B. Section IV, when used along with Section II, shows that there is an optimal collocation of PML variables and describes how those variables should be collocated on the mesh; and some helpful material is provided in Supplement C. Taken together, Sections III and IV describe the reconstruction problem where we start with facial variables and obtain those same variables at all locations on the mesh. Because this paper is focused on 2D, we describe the reconstruction problem in 2D, while pointing to places in the literature where the 3D reconstruction problem has been described. Section V describes the Implicit Taylor variant of ADER; again, there is helpful material in Supplement D. Specifically, we provide a formulation that is exceptionally well-suited for CED. The third algorithmic ingredient is the multidimensional Riemann solver which provides coupling across zones and allows for propagation of waves on these zones. This is described in Section VI. Section VII provides a pointwise description of how the entire PML for FVTD is implemented. Section VIII presents an optimization exercise for PML. Section IX presents conclusions.

II CPML EQUATIONS IN A FORMAT THAT IS SUITABLE FOR CONSTRAINT -PRESERVING FVTD/DGTD SCHEMES

A. Derivation of the CPML Equations

The globally constraint-preserving FVTD scheme is designated for ordinary Maxwell's equations, a.k.a Maxwellian equations, in which Maxwell's equations are written as a set of first-order linear partial differential equations. As a result, Maxwell's equations may be cast in flux form as detailed in Balsara *et al*. ([11]). Whereas this holds in many simple CED simulations, it is not relevant to complex cases in which Maxwell's equations are presented as a set of higher-order partial differential equations (a.k.a, non-Maxwellian equations) as in the case for CPML.

One common way to deal with this issue is to introduce some intermediate variables to transform the non-Maxwellian equations into a set of first-order partial differential equations which can be brought as close as possible to a flux form. However, this comes at the cost of introducing extra variables, i.e. auxiliary PML variables, which correspondingly leads to extra differential equations. Here, we follow the method first suggested by Roden & Gedney [38] and Gedney & Zhao [27] to convert the non-Maxwellian CPML equations into Maxwellian ones. This approach is based on the stretched-coordinate formulation.

Following the notation of Balsara *et al.* ([11], [12]), the time-harmonic Maxwell's curl equations in stretched-coordinate space are expressed as

$$+j\omega D_x = \frac{1}{s_y}\frac{\partial}{\partial y}\left(\frac{B_z}{\mu}\right) - \frac{1}{s_z}\frac{\partial}{\partial z}\left(\frac{B_y}{\mu}\right) \tag{2.1}$$

$$+j\omega D_y = \frac{1}{s_z}\frac{\partial}{\partial z}\left(\frac{B_x}{\mu}\right) - \frac{1}{s_x}\frac{\partial}{\partial x}\left(\frac{B_z}{\mu}\right) \tag{2.2}$$

$$+j\omega D_z = \frac{1}{s_x}\frac{\partial}{\partial x}\left(\frac{B_y}{\mu}\right) - \frac{1}{s_y}\frac{\partial}{\partial y}\left(\frac{B_x}{\mu}\right) \tag{2.3}$$

$$-j\omega B_x = \frac{1}{s_y}\frac{\partial}{\partial y}\left(\frac{D_z}{\varepsilon}\right) - \frac{1}{s_z}\frac{\partial}{\partial z}\left(\frac{D_y}{\varepsilon}\right) \tag{2.4}$$

$$-j\omega B_y = \frac{1}{s_z}\frac{\partial}{\partial z}\left(\frac{D_x}{\varepsilon}\right) - \frac{1}{s_x}\frac{\partial}{\partial x}\left(\frac{D_z}{\varepsilon}\right) \tag{2.5}$$

$$-j\omega B_z = \frac{1}{s_x}\frac{\partial}{\partial x}\left(\frac{D_y}{\varepsilon}\right) - \frac{1}{s_y}\frac{\partial}{\partial y}\left(\frac{D_x}{\varepsilon}\right) \tag{2.6}$$

where B_x, B_y and B_z are the x-, y-, and z -components of the magnetic flux density vector, and D_x, D_y, and D_z are the x-, y-, and z- components of the electric flux density vector. Also, ε and μ are permittivity and magnetic permeability, respectively. s_x, s_y, and s_z are the PML constitutive parameters defined as

$$s_x = \kappa_x + \frac{\sigma_x}{a_x + j\omega\varepsilon_0}; s_y = \kappa_y + \frac{\sigma_y}{a_y + j\omega\varepsilon_0};$$
$$s_z = \kappa_z + \frac{\sigma_z}{a_z + j\omega\varepsilon_0} \tag{2.7}$$

where σ_x, σ_y, σ_z represents the PML conductivity profile in each Cartesian direction, κ_x, κ_y, κ_z are the real parts of the PML constitutive parameters, and the role of a_x, a_y, and a_z is to shift the poles for the PML constitutive parameters off of the origin and into the upper-half complex plane.

The CPML equations (2.1) – (2.6) have a non-Maxwellian form in the time domain. To convert these equations into Maxwellian form, β_x, β_y, and β_z are introduced as follows

$$\frac{1}{s_x} = \frac{1}{\kappa_x} - \frac{1}{\beta_x};\ \frac{1}{s_y} = \frac{1}{\kappa_y} - \frac{1}{\beta_y};\ \frac{1}{s_z} = \frac{1}{\kappa_z} - \frac{1}{\beta_z} \tag{2.8}$$

Consider for the moment (2.1). Using (2.8), (2.1) may be written as

$$+j\omega D_x = \left(\frac{1}{\kappa_y} - \frac{1}{\beta_y}\right)\frac{\partial}{\partial y}\left(\frac{B_z}{\mu}\right) - \left(\frac{1}{\kappa_z} - \frac{1}{\beta_z}\right)\frac{\partial}{\partial z}\left(\frac{B_y}{\mu}\right) \tag{2.9}$$

Next, two auxiliary PML variables are introduced for (2.9)

$$Q^H_{y,z} = -\frac{1}{\beta_y}\frac{\partial}{\partial y}\left(\frac{B_z}{\mu}\right) \tag{2.10}$$

$$Q^H_{z,y} = -\frac{1}{\beta_z}\frac{\partial}{\partial z}\left(\frac{B_y}{\mu}\right) \tag{2.11}$$

where the superscript H in $Q^H_{y,z}$ denotes that the auxiliary variable corresponding to the magnetic field vector, the first subscript corresponds to the direction in which the PML is absorbing the wave, and the second subscript corresponds to the orientation of the H field component.

Using (2.10) and (2.11), (2.9) may now be expressed in the following form

$$+j\omega D_x = \frac{1}{\kappa_y}\frac{\partial}{\partial y}\left(\frac{B_z}{\mu}\right) - \frac{1}{\kappa_z}\frac{\partial}{\partial z}\left(\frac{B_y}{\mu}\right) + Q^H_{y,z} - Q^H_{z,y} \tag{2.12}$$

Expanding the first terms on the righthand side of (2.10) yields

$$\frac{1}{\beta_y} = \frac{1}{\kappa_y} - \frac{1}{s_y} = \frac{1}{\kappa_y} - \frac{1}{\kappa_y + \dfrac{\sigma_y}{a_y + j\omega\varepsilon_0}} = \frac{1}{\kappa_y}.\frac{\sigma_y}{\kappa_y\left(a_y + j\omega\varepsilon_0\right) + \sigma_y} \tag{2.13}$$

Plugging (2.13) into (2.10) and rearranging terms yields

$$\left(j\omega\right)Q^H_{y,z} + \frac{1}{\varepsilon_0}\frac{\sigma_y}{\kappa_y^2}.\frac{\partial}{\partial y}\left(\frac{B_z}{\mu}\right) = -\frac{1}{\varepsilon_0}\left(a_y + \frac{\sigma_y}{\kappa_y}\right)Q^H_{y,z} \tag{2.14}$$

The same approach may be applied to (2.11). As a result, (2.1) and its PML counterparts may be expressed in the time domain as

$$\frac{\partial}{\partial t}D_x = \frac{1}{\kappa_y}\frac{\partial}{\partial y}\left(\frac{B_z}{\mu}\right) - \frac{1}{\kappa_z}\frac{\partial}{\partial z}\left(\frac{B_y}{\mu}\right) + Q^H_{y,z} - Q^H_{z,y} \tag{2.15}$$

$$\frac{\partial}{\partial t}Q^H_{y,z} + \frac{1}{\varepsilon_0}\frac{\sigma_y}{\kappa_y^2}\frac{\partial}{\partial y}\left(\frac{B_z}{\mu}\right) = -\frac{1}{\varepsilon_0}\left(a_y + \frac{\sigma_y}{\kappa_y}\right)Q^H_{y,z} \tag{2.16}$$

$$\frac{\partial}{\partial t}Q^H_{z,y} + \frac{1}{\varepsilon_0}\frac{\sigma_z}{\kappa_z^2}\frac{\partial}{\partial z}\left(\frac{B_y}{\mu}\right) = -\frac{1}{\varepsilon_0}\left(a_z + \frac{\sigma_z}{\kappa_z}\right)Q^H_{z,y} \tag{2.17}$$

Applying the same approach to (2.2) – (2.6), the resulting set of Maxwell's equations in 3D with PML included, can be written. Supplement A provides the full set of detailed PML equations in physical space showing that they form a non-conservative hyperbolic system.

As detailed in Balsara *et al.* [11], writing the characteristic matrices from Supplement A allows us to perform a characteristic analysis of the wave speeds, which plays a crucial role in the implementation of the Reimann solvers in Section VI. Performing such a characteristic analysis here, the electromagnetic waves propagating in the *x*-, *y*-, and *z*-directions of the grid are found to propagate with the expected wave speeds, since the diagonal matrix of eigenvalues are

$$\boldsymbol{\Lambda}^x = diag\left(-c/\kappa_x, -c/\kappa_x, 0, \ldots, 0, +c/\kappa_x, +c/\kappa_x\right)_{18\,\mathrm{X}\,1} \quad (2.18)$$

$$\boldsymbol{\Lambda}^y = diag\left(-c/\kappa_y, -c/\kappa_y, 0, \ldots, 0, +c/\kappa_y, +c/\kappa_y\right)_{18\,\mathrm{X}\,1} \quad (2.19)$$

$$\boldsymbol{\Lambda}^z = diag\left(-c/\kappa_z, -c/\kappa_z, 0, \ldots, 0, +c/\kappa_z, +c/\kappa_z\right)_{18\,\mathrm{X}\,1} \quad (2.20)$$

Here "*c*" is the speed of light in vacuum. This completes our analysis of the CPML equations. (In a late stage of review, a referee pointed out the existence of other PML formulations Gedney *et al.* [26], Chen *et al.* [17] and Lu, Zhang and Cai [36] where the PML update equations have pure source terms, without any gradient terms. The ADER methods developed here are expressly suited to handling stiff source terms. Therefore, we do believe that the above-mentioned formulations would do substantially better with the ADER methods developed here, but it was too late to explore them in this paper.)

B. Parameter Specification for the CPML Equation

The PML parameters are designed to vary gradually in the PML region. This is done because any abrupt change in wave propagation characteristics can cause undue back-reflection of electromagnetic radiation. Therefore, we catalogue the method of setting up all the coefficients in one place. This will also be useful when these parameters have to be optimized in a later section so as to minimize back-reflection. For $\sigma^{\max}$ we set:

$$\sigma^{\max} = \frac{\sigma^{ref}\left(m+1\right)}{\eta_0\ \Delta x\ \sqrt{\varepsilon_r \mu_r}} \quad \text{with } \eta_0 = \sqrt{\frac{\mu_0}{\varepsilon_0}} = 376.72 \qquad (2.21)$$

where $3 \le m \le 4$ in the above equation, and ε_r and μ_r are relative permittivity and permeability. The PML layer ranges over $x_0 \le x \le x_0 + d$, where "*d*" is the thickness of the PML layer. The variation of the PML conductivity is given by

$$\sigma_x\left(x\right) = \begin{cases} \sigma^{\max}\left|\dfrac{x - x_0}{d}\right|^m & \text{for} \quad x_0 \le x \le x_0 + d \\ 0 & \text{otherwise} \end{cases} \qquad (2.22)$$

where again we use the same $3 \le m \le 4$ in the above equation. The above parameter has the dimensions of a physical conductivity. The next parameter can be interpreted as a scaling of the coordinate system, which means it is dimensionless.

$$\kappa_x\left(x\right) = \begin{cases} 1 + \left|\dfrac{x - x_0}{d}\right|^m \left(\kappa^{\max} - 1\right) & \text{for } x_0 \le x \le x_0 + d \\ 1 & \text{otherwise} \end{cases} \qquad (2.23)$$

where we also use the same $3 \le m \le 4$ in the above equation, and $\kappa^{\max} \ge 1$. Typically, $\kappa^{\max} \in \left[1, 25\right]$. The speed of light "*c*" decreases by a factor of $\kappa_x\left(x\right)$ in the PML region because $\kappa_x\left(x\right)$ multiplies both the permittivity and the permeability. The low-frequency behavior of the PML is also improved by shifting the pole away from the origin and into the lower half of the complex plane. This is accomplished by having

$$a_x\left(x\right) = \begin{cases} a^{\max}\left|\dfrac{x_0 + d - x}{d}\right| & \text{for} \quad x_0 \le x \le x_0 + d \\ 0 & \text{otherwise} \end{cases} \qquad (2.24)$$

Because of the relationship $s_x(x) = \kappa_x(x) + \sigma_x(x) / \left(a_x(x) + j\omega\varepsilon_0\right)$ we see that $a_x(x)$ has the same units as $\sigma_x(x)$. We also want $a_x(x_0 + \Delta x/2)$ to be much larger than $\sigma_x(x_0 + \Delta x/2)$ which is why the scaling goes in the opposite direction in the above equation.

Putting it all together, any PML can be specified by the distance "*d*", which is also the thickness of the PML layer as specified in number of zones. The further specification of the PML depends on specifying four numbers given by $\left(\sigma^{ref}, \kappa^{\max}, a^{\max}, m\right)$. These are the parameters we will use in our optimization study. Experience has shown that σ^{ref} and $\kappa^{\max}$ are the most important parameters. As a result, our optimization efforts will usually focus on these two parameters.

III. DIVERGENCE CONSTRAINT-PRESERVING RECONSTRUCTION OF CED VARIABLES

The facial electric and magnetic flux densities form the primal variables of the FVTD scheme. Divergence constraint-preserving FVTD, along with divergence constraint-preserving DGTD, relies on collocating the x-components of the electric and magnetic flux densities at the x-faces of the mesh. Likewise, the y-components of the electric and magnetic flux densities are collocated at the y-faces of the mesh and the z-components of the electric magnetic flux densities vectors are collocated at the z-faces of the mesh. It is important to realize that the divergence constraint couples all the components of the reconstructed vector field. One has, therefore, to treat the entire vector field as a single entity where the constraint causes the modes of one component to couple with the modes of the other components. Please see Fig. 1 from Balsara *et al.* [11] for a schematic diagram on how the vector fields are collocated on a zone. The PML variables in the next section follow the exact same collocation pattern.

The facial collocation of all the primal CED variables also suggests that they should be updated by using gradients of variables that are available at the edges of the mesh. Indeed, an examination of the CED equations from Section II would show that we just need the resolved states from two-dimensional Riemann solvers which are applied at the edges of the mesh in order to obtain an update strategy for the face-centered CED variables.

When the problem is restricted to two dimensions in the xy-plane, as it is out here, the z-components become zone-centered, while the x- and y-components still remain face-centered. Furthermore, in that two-dimensional limit, D_z and B_z should be treated as zone-centered variables that are to be updated with one-dimensional Riemann solvers.

The full three-dimensional divergence constraint-preserving reconstruction problem at second, third and fourth order of accuracy is described in Balsara *et al.* ([11], [12]). In this paper we use only the two-dimensional restrictions of the reconstruction problem. While this can be worked out, there are nuances in the reconstruction that enter into the ADER formulation. For this reason, Supplement B describes the two-dimensional divergence constraint-preserving reconstruction problem at second, third and fourth orders. The explicit presentation of the two-dimensional constraint-preserving reconstruction also gives the engineering community an easily accessible introduction to this topic.

IV. FACIALLY-MATCHING RECONSTRUCTION OF PML VARIABLES

The PML algorithm is intended to only act on a narrow layer of zones that is ten or so zones wide at the outer boundary of the computational domain. All the waves impinging on that layer should be absorbed in that layer. As a result, it is crucial to have a good collocation of variables for PML. An examination of the governing equations shows that we will have the best conformity between the CED variables and the PML variables if $Q^H_{y,z}, Q^H_{z,y}$ and $Q^E_{y,z}, Q^E_{z,y}$ are collocated at the x-faces of the mesh. An examination of the source terms for the update of D_x and B_x shows that the PML variables which are facially collocated in this fashion will have direct influence on the field variables that they are intended to suppress. Similarly, the update equations for $Q^H_{y,z}, Q^H_{z,y}$ and $Q^E_{y,z}, Q^E_{z,y}$ show that they are dependent only on the gradients in the y- and z-directions, giving us a further indication that it is best to collocate them in the x-faces. By examining the remaining PML equations we see that $Q^H_{z,x}, Q^H_{x,z}$ and $Q^E_{z,x}, Q^E_{x,z}$ should be collocated at the y-faces of the mesh. Likewise, $Q^H_{x,y}, Q^H_{y,x}$ and $Q^E_{x,y}, Q^E_{y,x}$ should be collocated at the z-faces of the mesh.

The facial collocation of all the PML variables also suggests that they should be updated by using gradients of variables that are available at the edges of the mesh. Indeed, an examination of the PML equations from Section II would show that we just need the resolved states from two-dimensional Riemann solvers which are applied at the edges of the mesh in order to obtain an update strategy for the face-centered PML variables. This will be further amplified in Section IV. Realize, therefore, that the update strategy for the PML variables has also been made very conformant with the update strategy for the face-centered components of the electric and magnetic flux densities. This allows us to make the most compact discretization of PML; which is good because the PML only acts on a thin layer of zones where it has to be maximally effective.

For two-dimensional problems that are restricted to the xy-plane we suppress all gradients in the z-direction. As a result, we can eliminate $Q^H_{z,x}$, $Q^H_{z,y}$, $Q^E_{z,y}$ and $Q^E_{z,x}$; so that we have just eight PML variables to consider instead of twelve in three-dimensions. Furthermore, in that two-dimensional limit, $Q^H_{x,y}, Q^H_{y,x}$ and $Q^E_{x,y}, Q^E_{y,x}$ should be treated as zone-centered variables that are to be updated with one-dimensional Riemann solvers.

Now realize that the PML update equations, along with the update equations for the regular CED, form a hyperbolic PDE system, albeit one with very stiff source terms. Because of the coupling between the two sets of equations via the source terms, the whole PDE system has to be treated as one entire system of equations. Therefore, if one is to design an “in-the-small” predictor step in the next section, the PML variables should also be reconstructed at all locations within any zone that is undergoing PML. But please realize that the PML variables are not required to be divergence-preserving. They are, nevertheless, required to be order preserving. In other words, the reconstruction strategy for PML must retain all the modes that are needed for the order property while also matching the facially collocated PML variables and their transverse variation in the faces of the mesh. Such a reconstruction strategy has been designed by Balsara, Samantaray and Subramanian [15] and is called the WENO-ADP reconstruction strategy. In other words, it draws on ideas from WENO (weighted essentially non-oscillatory) reconstruction while being ADP (almost divergence-preserving). In Balsara, Samantaray and Subramanian [15] we present the full 3D version of this algorithm from a mathematician’s perspective. Here we present the simplified version of the same, with some more helpful explanations and in two dimensions, to make it more accessible to engineers in Supplement C.

V. IMPLICIT TAYLOR ADER PREDICTOR FORMULATION FOR CED

We now focus on the Implicit Taylor variant of ADER (Arbitrary Accurate DERivatives), which was first formulated by Montecinos and Toro [33] and modified significantly with an eye to improving its utility by Montecinos and Balsara [34]. There is also the paper by Montecinos [35], but it does not construct as detailed expressions as this paper. We claim that this variant of ADER is optimally suited for CED. The PDE that is used in CED can be most easily written as

$$\mathbf{U}_t + \mathbf{A}\,\mathbf{U}_x + \mathbf{B}\,\mathbf{U}_y + \mathbf{C}\,\mathbf{U}_z = \mathbf{S}\,\mathbf{U} \tag{5.1}$$

Here $\mathbf{U}$ is the solution vector and $\mathbf{A}$, $\mathbf{B}$ and $\mathbf{C}$ are characteristic matrices which depend on the permittivity, permeability, σ and κ. The matrices vary slowly in space and do not vary in time; they are documented explicitly in Supplement A. The characteristic matrices are also solution-independent. As a result, they can be specified at any location within a zone. Furthermore, they vary only by small amounts within a zone with the result that we only need to retain linear variation with respect to space in the characteristic matrices. The source term $\mathbf{SU}$ is also linear in the solution vector $\mathbf{U}$. The matrix $\mathbf{S}$ depends on the conductivity and the conductivity can assume large values in metallic materials. Furthermore, the conductivity can have very large variation within a zone. Our goal will be to build a method that is uniquely adapted to the features of the PDE that governs CED calculations. We realize that the source terms can be so large that the solution method should be time-implicit in its treatment of the source terms. Furthermore, it is desirable to retain first derivatives in $\mathbf{S}$. It is also beneficial to a lesser extent to retain first derivatives in the characteristic matrices.

The full algorithm calls for a suitably high order spatial reconstruction step. This reconstruction gives us a high order representation of the solution within each zone. This is followed by a local predictor step applied within each zone. This predictor step gives us an “in-the-small” time-evolution of the solution based on the spatial variation within the zone. This time-evolution is made consistent with the governing equation in (5.1). The predictor step is then followed by the corrector step where the Riemann solvers are applied across zones and the time update is effected. The corrector step helps to connect the time-evolution across zones and is described later in Section VI. In this Section, we will first illustrate the construction of an Implicit Taylor ADER predictor formulation for CED in three dimensions and at second and third orders. We will then document the fourth order case in Supplement D, where only the final results are shown.

A. Second Order Implicit Taylor ADER Predictor Formulation

Using (5.1) we can write

$$\mathbf{U}_t = -\mathbf{A}\,\mathbf{U}_x - \mathbf{B}\,\mathbf{U}_y - \mathbf{C}\,\mathbf{U}_z + \mathbf{S}\,\mathbf{U} \tag{5.2}$$

In an Implicit Taylor expansion, we assume that we have the solution at some time $t=\tau$, where $\tau > 0$, and we relate it to the solution at $t=0$. Since we are propagating backward in time, the scheme becomes implicit. Since this is only a second order scheme, the backward Taylor series expansion gives

$$\mathbf{U}^{\tau} + (-\tau)\mathbf{U}_t^{\tau} = \mathbf{U}^{0} \tag{5.3}$$

Where the superscripts τ and 0 denote the time points at which the solution is evaluated. From (5.1), (5.2) and (5.3) we can write

$$\mathbf{U}^{\tau} = \mathbf{U}^{0} + \tau\left[-\mathbf{A}\mathbf{U}_x^{\tau} - \mathbf{B}\mathbf{U}_y^{\tau} - \mathbf{C}\mathbf{U}_z^{\tau} + \mathbf{S}\mathbf{U}^{\tau}\right] \tag{5.4}$$

Now realize that the unknowns in the above equation are $\mathbf{U}^{\tau}$, $\mathbf{U}_x^{\tau}$, $\mathbf{U}_y^{\tau}$ and $\mathbf{U}_z^{\tau}$. Clearly, (5.4) is only one equation, so it cannot give us all four of the above-mentioned vectors. We clearly need a trick to proceed. Now realize that (5.4) can be differentiated w.r.t. the x-coordinate and we realize that all second derivatives become zero in this second order approximation. The same can be done with all the other coordinate directions. The result is

$$\mathbf{U}_{\alpha}^{\tau} = \left[\mathbf{I} - \tau\mathbf{S}\right]^{-1}\mathbf{U}_{\alpha}^{0} \quad \text{where } \alpha = x, y, z \tag{5.5}$$

Once $\mathbf{U}_x^{\tau}$, $\mathbf{U}_y^{\tau}$ and $\mathbf{U}_z^{\tau}$ have been obtained using the above equation, we can easily find

$$\mathbf{U}^{\tau} = \left[\mathbf{I} - \tau\mathbf{S}\right]^{-1}\left\{\mathbf{U}^{0} + \tau\left[-\mathbf{A}\mathbf{U}_x^{\tau} - \mathbf{B}\mathbf{U}_y^{\tau} - \mathbf{C}\mathbf{U}_z^{\tau}\right]\right\} \tag{5.6}$$

This completes our description of the second order Implicit Taylor ADER predictor scheme.

B. Third Order Implicit Taylor ADER Predictor Formulation

We make the same assumption as was made for the derivation of the second order scheme. In other words, we assert the solution at some time $t=\tau$, where $\tau > 0$, and we relate it to the solution at $t=0$. Since we are propagating backward in time, the scheme becomes implicit. Because this is a third order scheme, the backward Taylor series expansion gives

$$\mathbf{U}^{\tau} + (-\tau)\,\mathbf{U}_t^{\tau} + (-\tau)^2\,\mathbf{U}_{tt}^{\tau}/2 = \mathbf{U}^{0}. \tag{5.7}$$

Where the superscripts τ and 0 denote the time points at which the solution is evaluated. Differentiating (5.1) with respect to the time variable t we obtain

$$\mathbf{U}_{tt} = -\mathbf{A}\left(\mathbf{U}_t\right)_x - \mathbf{B}\left(\mathbf{U}_t\right)_y - \mathbf{C}\left(\mathbf{U}_t\right)_z + \mathbf{S}\left(\mathbf{U}_t\right). \tag{5.8}$$

Now, using (5.2) in (5.8) we can obtain the following expression for $\mathbf{U}_{tt}$, which is independent of any temporal derivative terms:

$$\begin{aligned}\mathbf{U}_{tt} &= \mathbf{A}^2\,\mathbf{U}_{xx} + \mathbf{B}^2\,\mathbf{U}_{yy} + \mathbf{C}^2\,\mathbf{U}_{zz} + \langle\mathbf{AB}\rangle\,\mathbf{U}_{xy} + \langle\mathbf{BC}\rangle\,\mathbf{U}_{yz} \\ &\quad + \langle\mathbf{AC}\rangle\,\mathbf{U}_{xz} + \left(\langle\partial\mathbf{A}\rangle - \langle\mathbf{AS}\rangle\right)\mathbf{U}_x + \left(\langle\partial\mathbf{B}\rangle - \langle\mathbf{BS}\rangle\right)\mathbf{U}_y \\ &\quad + \left(\langle\partial\mathbf{C}\rangle - \langle\mathbf{CS}\rangle\right)\mathbf{U}_z + \left(\mathbf{S}^2 - \langle\partial\mathbf{S}\rangle\right)\mathbf{U}\end{aligned} \tag{5.9}$$

where we have used the following compact forms which enables us to have a very compact notation

$\langle\mathbf{AB}\rangle \equiv \mathbf{AB} + \mathbf{BA}$; $\langle\partial\mathbf{S}\rangle \equiv \mathbf{AS}_x + \mathbf{BS}_y + \mathbf{CS}_z$;

$\langle\partial_x\mathbf{S}\rangle \equiv \mathbf{A}_x\mathbf{S}_x + \mathbf{B}_x\mathbf{S}_y + \mathbf{C}_x\mathbf{S}_z$; $\langle\partial_y\mathbf{S}\rangle \equiv \mathbf{A}_y\mathbf{S}_x + \mathbf{B}_y\mathbf{S}_y + \mathbf{C}_y\mathbf{S}_z$;

$\langle\partial_z\mathbf{S}\rangle \equiv \mathbf{A}_z\mathbf{S}_x + \mathbf{B}_z\mathbf{S}_y + \mathbf{C}_z\mathbf{S}_z$; for any matrix $\mathbf{S}$

$\langle P_3\mathbf{S}^{-1}\rangle \equiv \left[\mathbf{I} - \tau\mathbf{S} + \frac{1}{2}\tau^2\mathbf{S}^2\right]^{-1}$ where "P_3" stands for the Pade approximation at 3rd order.

$\langle\tau_3\mathbf{A}\rangle \equiv \tau\mathbf{A} - \tau^2\langle\mathbf{AS}\rangle/2$; $\langle\tau_3\mathbf{B}\rangle \equiv \tau\mathbf{B} - \tau^2\langle\mathbf{BS}\rangle/2$;

$\langle\tau_3\mathbf{C}\rangle \equiv \tau\mathbf{C} - \tau^2\langle\mathbf{CS}\rangle/2$

From (5.2), (5.7) and (5.9) we can write

$$\mathbf{U}^{\tau} = \mathbf{U}^{0} + \tau\left[-\mathbf{A}\mathbf{U}_{x}^{\tau} - \mathbf{B}\mathbf{U}_{y}^{\tau} - \mathbf{C}\mathbf{U}_{z}^{\tau} + \mathbf{S}\mathbf{U}^{\tau}\right] - \frac{1}{2}\tau^{2}\begin{bmatrix} \mathbf{A}^{2}\mathbf{U}_{xx}^{\tau} + \mathbf{B}^{2}\mathbf{U}_{yy}^{\tau} + \mathbf{C}^{2}\mathbf{U}_{zz}^{\tau} + \langle\mathbf{AB}\rangle\mathbf{U}_{xy}^{\tau} + \langle\mathbf{BC}\rangle\mathbf{U}_{yz}^{\tau} \\ + \langle\mathbf{AC}\rangle\mathbf{U}_{xz}^{\tau} + \left(\langle\partial\mathbf{A}\rangle - \langle\mathbf{AS}\rangle\right)\mathbf{U}_{x}^{\tau} + \left(\langle\partial\mathbf{B}\rangle - \langle\mathbf{BS}\rangle\right)\mathbf{U}_{y}^{\tau} \\ + \left(\langle\partial\mathbf{C}\rangle - \langle\mathbf{CS}\rangle\right)\mathbf{U}_{z}^{\tau} + \left(\mathbf{S}^{2} - \langle\partial\mathbf{S}\rangle\right)\mathbf{U}^{\tau} \end{bmatrix}. \tag{5.10}$$

Now realize that the unknowns in the above equations are $\mathbf{U}^{\tau}$ $\mathbf{U}_{x}^{\tau}$, $\mathbf{U}_{y}^{\tau}$, $\mathbf{U}_{z}^{\tau}$ $\mathbf{U}_{xx}^{\tau}$, $\mathbf{U}_{yy}^{\tau}$, $\mathbf{U}_{zz}^{\tau}$, $\mathbf{U}_{xy}^{\tau}$, $\mathbf{U}_{yz}^{\tau}$ and $\mathbf{U}_{xz}^{\tau}$. Clearly, (5.10) is only one equation, so it cannot give us all ten of the above-mentioned vectors. We clearly need a trick similar to the one used for the second order derivation, to proceed. Now realize that (5.10) can be differentiated with respect to the x-coordinate to obtain the following expression:

$$\mathbf{U}_{x}^{\tau} = \mathbf{U}_{x}^{0} + \tau\begin{bmatrix} -\mathbf{A}\mathbf{U}_{xx}^{\tau} - \mathbf{B}\mathbf{U}_{xy}^{\tau} - \mathbf{C}\mathbf{U}_{xz}^{\tau} + \mathbf{S}\mathbf{U}_{x}^{\tau} \\ -\mathbf{A}_{x}\mathbf{U}_{x}^{\tau} - \mathbf{B}_{x}\mathbf{U}_{y}^{\tau} - \mathbf{C}_{x}\mathbf{U}_{z}^{\tau} + \mathbf{S}_{x}\mathbf{U}^{\tau} \end{bmatrix} - \frac{1}{2}\tau^{2} \begin{bmatrix} \left(\langle\mathbf{A}_{x}\mathbf{A}\rangle + \langle\partial\mathbf{A}\rangle - \langle\mathbf{AS}\rangle\right)\mathbf{U}_{xx}^{\tau} + \langle\mathbf{B}_{x}\mathbf{B}\rangle\mathbf{U}_{yy}^{\tau} \\ + \langle\mathbf{C}_{x}\mathbf{C}\rangle\mathbf{U}_{zz}^{\tau} + \left(\langle\mathbf{A}_{x}\mathbf{B}\rangle + \langle\partial\mathbf{B}\rangle + \langle\mathbf{B}_{x}\mathbf{A}\rangle + \langle\mathbf{BS}\rangle\right)\mathbf{U}_{xy}^{\tau} \\ + \left(\langle\mathbf{B}_{x}\mathbf{C}\rangle + \langle\mathbf{BC}_{x}\rangle\right)\mathbf{U}_{yz}^{\tau} + \begin{pmatrix} \langle\mathbf{A}_{x}\mathbf{C}\rangle + \langle\mathbf{AC}_{x}\rangle \\ + \langle\partial\mathbf{C}\rangle - \langle\mathbf{CS}\rangle \end{pmatrix}\mathbf{U}_{xz}^{\tau} \\ + \left(\langle\partial_{x}\mathbf{A}\rangle - \langle\mathbf{A}_{x}\mathbf{S}\rangle - \langle\mathbf{AS}_{x}\rangle + \mathbf{S}^{2} - \langle\partial\mathbf{S}\rangle\right)\mathbf{U}_{x}^{\tau} \\ + \left(\langle\partial_{x}\mathbf{B}\rangle - \langle\mathbf{B}_{x}\mathbf{S}\rangle - \langle\mathbf{BS}_{x}\rangle\right)\mathbf{U}_{y}^{\tau} + \begin{pmatrix} \langle\partial_{x}\mathbf{C}\rangle - \langle\mathbf{C}_{x}\mathbf{S}\rangle \\ -\langle\mathbf{CS}_{x}\rangle \end{pmatrix}\mathbf{U}_{z}^{\tau} \\ + \left(\langle\mathbf{S}_{x}\mathbf{S}\rangle - \langle\partial_{x}\mathbf{S}\rangle\right)\mathbf{U}^{\tau} \end{bmatrix} \tag{5.11}$$

Note that to obtain the above expression we have suppressed all the second-order derivatives of $\mathbf{S}$. Now we can greatly simplify the expression for $\mathbf{U}_{x}^{\tau}$ from that of (5.11) if we ignore all the gradients of $\mathbf{A}$, $\mathbf{B}$, $\mathbf{C}$ and $\mathbf{S}$. This allows us to keep only the terms that dominate in the evolution of the gradient of the solution. The gradient of the solution is not one of the primary desiderata of the method, but it is essential for the overall implementation of the method. So, this choice is justified. This approximation enables us to get

$$\mathbf{U}_{x}^{\tau} = \mathbf{U}_{x}^{0} + \tau\mathbf{S}\mathbf{U}_{x}^{\tau} - \frac{1}{2}\tau^{2}\mathbf{S}^{2}\mathbf{U}_{x}^{\tau} - \langle\tau_{3}\mathbf{A}\rangle\mathbf{U}_{xx}^{\tau} - \langle\tau_{3}\mathbf{B}\rangle\mathbf{U}_{xy}^{\tau} - \langle\tau_{3}\mathbf{C}\rangle\mathbf{U}_{xz}^{\tau} \quad .(5.12)$$

Similarly, the derivatives in the y- and z- directions are given by

$$\mathbf{U}_{y}^{\tau} = \mathbf{U}_{y}^{0} + \tau\mathbf{S}\mathbf{U}_{y}^{\tau} - \frac{1}{2}\tau^{2}\mathbf{S}^{2}\mathbf{U}_{y}^{\tau} - \langle\tau_{3}\mathbf{A}\rangle\mathbf{U}_{xy}^{\tau} - \langle\tau_{3}\mathbf{B}\rangle\mathbf{U}_{yy}^{\tau} - \langle\tau_{3}\mathbf{C}\rangle\mathbf{U}_{yz}^{\tau};$$
$$\mathbf{U}_{z}^{\tau} = \mathbf{U}_{z}^{0} + \tau\mathbf{S}\mathbf{U}_{z}^{\tau} - \frac{1}{2}\tau^{2}\mathbf{S}^{2}\mathbf{U}_{z}^{\tau} - \langle\tau_{3}\mathbf{A}\rangle\mathbf{U}_{xz}^{\tau} - \langle\tau_{3}\mathbf{B}\rangle\mathbf{U}_{yz}^{\tau} - \langle\tau_{3}\mathbf{C}\rangle\mathbf{U}_{zz}^{\tau}. \tag{5.13}$$

Retaining the assumption that all the linear variations in $\mathbf{A}$, $\mathbf{B}$, $\mathbf{C}$ and $\mathbf{S}$ are suppressed, we can differentiate (5.12) once more to obtain

$$\mathbf{U}_{xx}^{\tau} = \mathbf{U}_{xx}^{0} + \tau\mathbf{S}\mathbf{U}_{xx}^{\tau} - \frac{1}{2}\tau^{2}\mathbf{S}^{2}\mathbf{U}_{xx}^{\tau}. \tag{5.14}$$

Now solving for $\mathbf{U}_{xx}^{\tau}$, from (5.14) we get

$$\mathbf{U}_{xx}^{\tau} = \left\langle P_{3}\mathbf{S}^{-1}\right\rangle\mathbf{U}_{xx}^{0}. \tag{5.15}$$

Analogously we obtain five more expressions from

$$\mathbf{U}_{\alpha\beta}^{\tau} = \left\langle P_{3}\mathbf{S}^{-1}\right\rangle\mathbf{U}_{\alpha\beta}^{0} \quad \text{with } \alpha = x,y,z \text{ and } \beta = x,y,z \tag{5.16}$$

Equations (5.15) and (5.16) give us explicit values for $\mathbf{U}_{xx}^{\tau}$, $\mathbf{U}_{yy}^{\tau}$, $\mathbf{U}_{zz}^{\tau}$, $\mathbf{U}_{xy}^{\tau}$, $\mathbf{U}_{yz}^{\tau}$ and $\mathbf{U}_{xz}^{\tau}$. Once these second derivative terms are obtained, they can be substituted in (5.12) and (5.13) to get simple expressions for the first derivatives as follows:

$$\mathbf{U}_{x}^{\tau} = \left\langle P_{3}\mathbf{S}^{-1}\right\rangle\left\{\mathbf{U}_{x}^{0} - \langle\tau_{3}\mathbf{A}\rangle\mathbf{U}_{xx}^{\tau} - \langle\tau_{3}\mathbf{B}\rangle\mathbf{U}_{xy}^{\tau} - \langle\tau_{3}\mathbf{C}\rangle\mathbf{U}_{xz}^{\tau}\right\};$$
$$\mathbf{U}_{y}^{\tau} = \left\langle P_{3}\mathbf{S}^{-1}\right\rangle\left\{\mathbf{U}_{y}^{0} - \langle\tau_{3}\mathbf{A}\rangle\mathbf{U}_{xy}^{\tau} - \langle\tau_{3}\mathbf{B}\rangle\mathbf{U}_{yy}^{\tau} - \langle\tau_{3}\mathbf{C}\rangle\mathbf{U}_{yz}^{\tau}\right\}; \tag{5.17}$$
$$\mathbf{U}_{z}^{\tau} = \left\langle P_{3}\mathbf{S}^{-1}\right\rangle\left\{\mathbf{U}_{z}^{0} - \langle\tau_{3}\mathbf{A}\rangle\mathbf{U}_{xz}^{\tau} - \langle\tau_{3}\mathbf{B}\rangle\mathbf{U}_{yz}^{\tau} - \langle\tau_{3}\mathbf{C}\rangle\mathbf{U}_{zz}^{\tau}\right\}.$$

Once the linear variations $\mathbf{U}_{x}^{\tau}$, $\mathbf{U}_{y}^{\tau}$ and $\mathbf{U}_{z}^{\tau}$ have been obtained, we can assemble all the terms in (5.10) to obtain $\mathbf{U}^{\tau}$ explicitly as:

$$\mathbf{U}^{\tau} = \left[\mathbf{I} - \tau\mathbf{S} + \frac{1}{2}\tau^{2}(\mathbf{S}^{2} - \langle\partial\mathbf{S}\rangle)\right]^{-1} \left\{\begin{matrix} \mathbf{U}^{0} - \left[\langle\tau_{3}\mathbf{A}\rangle + \frac{1}{2}\tau^{2}\langle\partial\mathbf{A}\rangle\right]\mathbf{U}_{x}^{\tau} - \left[\langle\tau_{3}\mathbf{B}\rangle + \frac{1}{2}\tau^{2}\langle\partial\mathbf{B}\rangle\right]\mathbf{U}_{y}^{\tau} \\ -\left[\langle\tau_{3}\mathbf{C}\rangle + \frac{1}{2}\tau^{2}\langle\partial\mathbf{C}\rangle\right]\mathbf{U}_{z}^{\tau} - \frac{1}{2}\tau^{2}\mathbf{A}^{2}\mathbf{U}_{xx}^{\tau} - \frac{1}{2}\tau^{2}\mathbf{B}^{2}\mathbf{U}_{yy}^{\tau} \\ -\frac{1}{2}\tau^{2}\mathbf{C}^{2}\mathbf{U}_{zz}^{\tau} - \frac{1}{2}\tau^{2}\langle\mathbf{AB}\rangle\mathbf{U}_{xy}^{\tau} - \frac{1}{2}\tau^{2}\langle\mathbf{BC}\rangle\mathbf{U}_{yz}^{\tau} - \frac{1}{2}\tau^{2}\langle\mathbf{AC}\rangle\mathbf{U}_{xz}^{\tau} \end{matrix}\right\} \tag{5.18}$$

The above expression is designed to minimize the number of matrix-vector multiplication steps. The square matrices, indicated by the square brackets in the above equation, can be pre-computed for each zone and re-used, if one wishes. In many useful limits that arise in CED, the inverse can also be analytically pre-computed using a computer algebra system.

This completes our description of the third order Implicit Taylor ADER predictor scheme.

It is advantageous to extract some essential insights about the Implicit Taylor ADER predictor algorithm and its treatment of source terms with increasing order of accuracy. To that end, ignore the spatial variation of the source terms and inter-compare the matrix $\left[\mathbf{I}-\tau\mathbf{S}\right]^{-1}$ in (5.5) and (5.6), the matrix $\left[\mathbf{I}-\tau\mathbf{S}+\frac{1}{2}\tau^2\mathbf{S}^2\right]^{-1}$ in (5.15) to (5.18) and then the matrix $\left[\mathbf{I}-\tau\mathbf{S}+\frac{1}{2}\tau^2\mathbf{S}^2-\frac{1}{6}\tau^3\mathbf{S}^3\right]^{-1}$ in (D.3) to (D.8). We see that they are successively high order Padé approximations for the fully implicit treatment of the equation $\mathbf{U}_t=\mathbf{S}\,\mathbf{U}$, where the source terms, $\mathbf{S}\mathbf{U}$, can be stiff. Since the Padé approximations are optimal up to the desired order, we realize that the Implicit Taylor ADER predictor algorithm is optimal for the treatment of stiff source terms by its very design. In other words, it is ideally suited for CED applications where the stiff source terms are of the form $\mathbf{S}\mathbf{U}$ with the matrix $\mathbf{S}$ having zero or negative eigenvalues. Another useful insight would be to note that in large parts of the computational domain, the source terms might be zero. In that limit, and in those zones, the matrix inversion becomes unnecessary and the method becomes even more efficient. In fact, it becomes as efficient as an Explicit Taylor version of ADER. For those who are mathematically inclined and know the previous literature, another insight is also worthwhile. Realize that, compared with the conventional Implicit ADER of Toro and Montecinos [44], this approach should be superior, mainly because this formulation decouples the algebraic equations for state and derivatives in sub-problems where the same matrix inversion is required.

C. Implementation of the Implicit Taylor ADER Algorithm at Second Order

In this and the next sections (and in Supplement D. *II*) we consider the ADER algorithm applied to a zone of extent Δx and Δy in the two spatial directions. In that zone we want to build an "in-the-small" predictor step with a timestep Δt. The first thing to realize is that we have to identify the suitable temporal quadrature points for each order of accuracy; these are obtained based on Gaussian quadrature. For second order accurate evolution we only need one quadrature point which is at the middle of the timestep. But to obtain an efficient implementation it helps to go from the physical space-time element $\left[-\Delta x/2,\Delta x/2\right]\times\left[-\Delta y/2,\Delta y/2\right]\times\left[0,\Delta t\right]$ to the reference element in space-time given by $\left[-1/2,1/2\right]\times\left[-1/2,1/2\right]\times\left[0,1\right]$. Since we have only one temporal quadrature point at second order, we define $\tau_1=1/2$ in the reference element. To obtain an "in-the-small" predictor step we would like to have the entire reconstruction polynomial at time τ_1.

We can achieve the goal of obtaining the entire reconstruction polynomial at time τ_1 by using all the results from Sub-Section V.*A*. But first we have to address two further issues. First, we need to understand how (5.5) and (5.6) get modified when recast in the reference space-time element. It is easy to see that the transformation of variables requires us to make the transcription

$$\mathbf{A}\rightarrow\frac{\Delta t}{\Delta x}\mathbf{A}\;\;;\;\;\mathbf{B}\rightarrow\frac{\Delta t}{\Delta y}\mathbf{B}\;\;;\;\;\mathbf{S}\rightarrow\Delta t\;\mathbf{S} \qquad (5.19)$$

With this transcription, we can set $\tau_1=1/2$ in (5.5) and (5.6). Second, we need to learn how to go from the reconstruction in (B.6), (B.7) and (C.2), which is only available at $\tau=0$, to the state $\mathbf{U}^{\tau}$ and the derivatives $\mathbf{U}_x^{\tau_1}$ and $\mathbf{U}_y^{\tau_1}$ at the advanced time. The important insight is that in two dimensions $\mathbf{U}^{\tau_1}$ is a 14 component column vector written as $\left(D_x,D_y,D_z,B_x,B_y,B_z,Q^H_{y,z},Q^H_{x,y},Q^H_{x,z},Q^H_{y,x},Q^E_{y,z},Q^E_{x,y},Q^E_{x,z},Q^E_{y,x}\right)^T$. But realize from (B.6), (B.7) that the electric and magnetic flux density terms can have quadratic variations of the form $\left(x^2-1/12\right)$, $\left(y^2-1/12\right)$ and xy. Furthermore, from (C.2) we know that the remaining eight terms may also have variations of the form xy. We, therefore, realize that $\mathbf{U}^0$ and the derivatives $\mathbf{U}_x^0$ and $\mathbf{U}_y^0$ at $\tau=0$ can be obtained at the zone center by differentiation of equations like (B.6), (B.7) and (C.2). Furthermore, because of the extra terms in (B.6), (B.7) and (C.2), we can also obtain $\mathbf{U}_{xx}^0$, $\mathbf{U}_{yy}^0$ and $\mathbf{U}_{xy}^0$ at $\tau=0$ and we should account for their time-evolution.

Once $\mathbf{U}^0$, $\mathbf{U}_x^0$, $\mathbf{U}_y^0$, $\mathbf{U}_{xx}^0$, $\mathbf{U}_{yy}^0$ and $\mathbf{U}_{xy}^0$ are in hand, we can extend (5.5) to obtain

$$\mathbf{U}_{\alpha\beta}^{\tau_1}=\left[\mathbf{I}-\tau_1\mathbf{S}\right]^{-1}\mathbf{U}_{\alpha\beta}^0\;\;;\qquad\alpha,\beta\in\{x,y\} \qquad (5.20)$$

We use these in addition to (5.5) and (5.6) with $\tau=\tau_1$ to obtain $\mathbf{U}^{\tau_1}$, $\mathbf{U}_x^{\tau_1}$, $\mathbf{U}_y^{\tau_1}$, $\mathbf{U}_{xx}^{\tau_1}$, $\mathbf{U}_{yy}^{\tau_1}$ and $\mathbf{U}_{xy}^{\tau_1}$. With these time-advanced derivatives in hand, we can obtain the predicted solution at any face-centered or edge-centered quadrature point at which we may want to apply a 1D or 2D Riemann solver. In other words, this predictor step has given us the spatially and temporally second order accurate predicted solution which can now be used to obtain the input states for the Riemann solvers. It also gives us the fully time-implicit source terms, evaluated from within the zone of interest, at each of the faces of that zone. The final facial source terms that are needed for the one stage update of the facial variables will then be obtained via arithmetic averaging from each of the two zones that abut the face; and this will be described in further detail in Section VII. This completes our description of the ADER predictor step at second order.

D. Implementation of the Implicit Taylor ADER Algorithm at Third Order

At third order, the transcription from physical space-time element to the reference element is unchanged. Similarly, (5.19) is also unchanged. At third order we have two quadrature points given by $\tau_1 = \left(1 - 1/\sqrt{3}\right)/2$ and $\tau_2 = \left(1 + 1/\sqrt{3}\right)/2$. There are other nuances that we encounter at third order, and we address them next.

Now realize that permittivity, permeability and conductivity, as well as PML parameters, can indeed vary with spatial location within a zone. But they do not vary with time. Therefore, at third order and beyond, we have also to account for the spatial derivatives of the matrices $\mathbf{A}$, $\mathbf{B}$ and $\mathbf{S}$, though we do not need to account for their time derivatives. We do that simply via finite differencing. Let us illustrate with a simple example. Let $\mathbf{A}_R$ and $\mathbf{A}_L$ be the matrices for $\mathbf{A}$ at the right and left boundaries of the zone being considered. Similarly, let $\mathbf{A}_U$ and $\mathbf{A}_D$ be the matrices for $\mathbf{A}$ at the up and down boundaries of the zone being considered. We can then write

$$\mathbf{A}_x = \left(\mathbf{A}_R - \mathbf{A}_L\right)/\Delta x \;\; ; \;\; \mathbf{A}_y = \left(\mathbf{A}_U - \mathbf{A}_D\right)/\Delta y \qquad (5.21)$$

Therefore, the gradients of the matrices that we are considering also become important at third order and beyond. The big benefit of including these gradients is that they allow us to account for variation in material properties within a zone; i.e. a kind of sub-cell resolution. We will see later on that this sub-cell resolution helps us in obtaining superior late-time behavior in the PML at higher orders.

Now recall from scanning the reconstructed modes in Supplement B. *II* and Supplement C. *II* that in addition to modes with quadratic variation we will have modes with cubic variation. Therefore, at the center of the zone, and at time $\tau = 0$ we can obtain $\mathbf{U}^0$, $\mathbf{U}^0_x$, $\mathbf{U}^0_y$, $\mathbf{U}^0_{xx}$, $\mathbf{U}^0_{yy}$, $\mathbf{U}^0_{xy}$, $\mathbf{U}^0_{xxx}$, $\mathbf{U}^0_{yyy}$, $\mathbf{U}^0_{xxy}$ and $\mathbf{U}^0_{xyy}$. Using these, our task is to obtain $\mathbf{U}^\tau$, $\mathbf{U}^\tau_x$, $\mathbf{U}^\tau_y$, $\mathbf{U}^\tau_{xx}$, $\mathbf{U}^\tau_{yy}$, $\mathbf{U}^\tau_{xy}$, $\mathbf{U}^\tau_{xxx}$, $\mathbf{U}^\tau_{yyy}$, $\mathbf{U}^\tau_{xxy}$ and $\mathbf{U}^\tau_{xyy}$ at scaled times $\tau = \tau_1$ and $\tau = \tau_2$. As in the second order case, we extend (5.15) to write

$$\mathbf{U}^\tau_{\alpha\beta\gamma} = \left\langle P_3 \mathbf{S}^{-1} \right\rangle \mathbf{U}^0_{\alpha\beta\gamma}; \quad \alpha, \beta, \gamma \in \{x, y\} \qquad (5.22)$$

We can assert (5.15), to (5.18), along with (5.22) at scaled times $\tau = \tau_1$ and $\tau = \tau_2$ to obtain our desired result. With these time-advanced derivatives in hand, we can obtain the predicted solution at any face-centered or edge-centered spatial quadrature point at which we may want to apply a 1D or 2D Riemann solver. For CED, the material properties do not evolve in time. We can, therefore, make the simplification of using time-integrated states at the spatial quadrature points where we want to invoke these Riemann solvers. That reduces the number of Riemann solvers that need to be invoked. This step also gives us the fully time-implicit source terms, evaluated from within the zone of interest, at each of the faces of that zone.

VI. TWO-DIMENSIONAL RIEMANN SOLVER AND ITS ROLE IN THE SINGLE STAGE CORRECTOR STEP

We first describe the two-dimensional Riemann solver whilst putting it in context with the reconstruction and predictor steps from Sections III, IV and V. We then describe the single stage corrector step.

A. Description of the Two-Dimensional Riemann Solver

Multidimensional Riemann solvers that are practical and easy to implement were first worked out in Balsara [5], [6], [7] and Balsara and Nkonga [10]. For CED applications, the structure of the multidimensional Riemann solver becomes even simpler because of two reasons:- First, the system is linear and second, there are symmetries that we can exploit in the update equations. We describe the multidimensional Riemann solver with all the simplifications incorporated in this Section. This also gives us insight into the time-update strategy that is used in the corrector step.

Consider the set of equations described in (2.15), (2.16) and (2.17) and please focus on the parts that correspond to spatial gradients in those equations. We see from (2.15) that the corrector step update of D_x in (2.15) requires the two gradients $\partial\left(B_z/\mu\right)/\partial y$ and $\partial\left(B_y/\mu\right)/\partial z$. The gradients can be evaluated in the x-faces where D_x is collocated. Now realize that the corrector step update of $Q^H_{y,z}$ in (2.16) relies only on one of the two previous gradients, $\partial\left(B_z/\mu\right)/\partial y$. Also recall that $Q^H_{y,z}$ is also collocated in the same x-faces. Also realize that the corrector step update of $Q^H_{z,y}$ in (2.17) relies only on the other of the two previous gradients, $\partial\left(B_y/\mu\right)/\partial z$. Therefore, if we have a physically motivated (i.e. multidimensionally upwinded) strategy for obtaining B_z variables at the z-edges of the mesh and B_y variables at the y-edges of the mesh, it would then be easy to update (2.15), (2.16) and (2.17) in the corrector step. The coefficients in front of the gradient terms in (2.15), (2.16) and (2.17) are time-independent and can be spatially averaged at the x-faces of the mesh when carrying out the corrector step. By examining the full equation set in (A.1) to (A.18) we realize that a similar consideration can be applied to each of the matched triplets of update equations.

To obtain the desired accuracy in space and time for the update in the corrector step, we only need to use the previously-described numerical algorithms as follows. Using Sections III and IV, we reconstruct all variables with the desired spatial accuracy. Then using Section V we can make a matching, temporally high order accurate, in-the-small, time-

$\mathbf{U}_{RU}$, $\mathbf{U}_{LU}$, $\mathbf{U}_{LD}$ and $\mathbf{U}_{RD}$ that come together at the z-edge. The z-edge is seen from above in Fig. 1a as the thick dot and we also see the four zones that lie in the xy-plane. The subscripts "RU", "LU", "LD" and "RD" denote the Right-Up, Left-Up, Left-Down and Right-Down zones. Since we have the accurate space and time evolution within each of the four zones shown in Fig. 1a, the four states $\mathbf{U}_{RU}$, $\mathbf{U}_{LU}$, $\mathbf{U}_{LD}$ and $\mathbf{U}_{RD}$ can be evaluated at the z-edge with the desired spatial and temporal accuracy. These four states form the input states of the multidimensional Riemann solver.

The task of the multidimensional Riemann solver shown in Fig. 1a is to produce a unique resolved state at the z-edge shown in Fig. 1a. Specifically, at the z-edge we only want D_z and B_z. Notice that at no point in the update of (A.1) to (A.18) will we need the PML "Q" variables at any of the edges. This allows us to restrict our focus to a much smaller 6×6 hyperbolic system given by

$$\frac{\partial}{\partial t}\begin{pmatrix} D_x \\ D_y \\ D_z \\ B_x \\ B_y \\ B_z \end{pmatrix} + \frac{\partial}{\partial x}\begin{pmatrix} 0 \\ B_z/(\kappa_x \mu) \\ -B_y/(\kappa_x \mu) \\ 0 \\ -D_z/(\kappa_x \varepsilon) \\ D_y/(\kappa_x \varepsilon) \end{pmatrix} + \frac{\partial}{\partial y}\begin{pmatrix} -B_z/(\kappa_y \mu) \\ 0 \\ B_x/(\kappa_y \mu) \\ D_z/(\kappa_y \varepsilon) \\ 0 \\ -D_x/(\kappa_y \varepsilon) \end{pmatrix}$$
$$+\frac{\partial}{\partial z}\begin{pmatrix} B_y/(\kappa_z \mu) \\ -B_x/(\kappa_z \mu) \\ 0 \\ -D_y/(\kappa_z \varepsilon) \\ D_x/(\kappa_z \varepsilon) \\ 0 \end{pmatrix} = \begin{pmatrix} Q^H_{y,z} - Q^H_{z,y} \\ Q^H_{z,x} - Q^H_{x,z} \\ Q^H_{x,y} - Q^H_{y,x} \\ -Q^E_{y,z} + Q^E_{z,y} \\ -Q^E_{z,x} + Q^E_{x,z} \\ -Q^E_{x,y} + Q^E_{y,x} \end{pmatrix} \tag{6.1}$$

The x-, y- and z-directional fluxes in the above equation will be denoted by **F**, **G** and **H**. When working with the multidimensional Riemann solver we only restrict attention to the above six-component system. The source terms on the right hand side of (6.1) do not contribute to the Riemann solver; though they will contribute to the eventual corrector step. An examination of the x-flux shows us, see (2.18), that the waves propagate symmetrically in the x-direction with right- and left-going speeds $S_R = c/\kappa_x$ and $-S_R = -c/\kappa_x$. Likewise, an examination of the y-flux shows us, see (2.19), that the waves propagate symmetrically in the y-direction with up- and down-going speeds $S_U = c/\kappa_y$ and $-S_U = -c/\kappa_y$. These speeds do contribute to the multidimensional Riemann solver, as shown in Fig. 1b.

Between the states $\mathbf{U}_{RU}$ and $\mathbf{U}_{LU}$, we have the formation of a one-dimensional Riemann problem in the x-direction with a resolved state $\mathbf{U}^*_U$, as shown in Fig. 1b, and given explicitly by

$$\mathbf{U}^*_U = \frac{1}{2}\left(\mathbf{U}_{RU} + \mathbf{U}_{LU}\right) - \frac{1}{2S_R}\left(\mathbf{F}\left(\mathbf{U}_{RU}\right) - \mathbf{F}\left(\mathbf{U}_{LU}\right)\right) \tag{6.2}$$

From the state $\mathbf{U}^*_U$ we can also obtain the y-flux $\mathbf{G}\left(\mathbf{U}^*_U\right)$. Between the states $\mathbf{U}_{RD}$ and $\mathbf{U}_{LD}$, we have the formation of a one-dimensional Riemann problem in the x-direction with a resolved state $\mathbf{U}^*_D$, as shown in Fig. 1b. To obtain $\mathbf{U}^*_D$, just replace $U \to D$ in (6.2). From the state $\mathbf{U}^*_D$ we can also obtain the y-flux $\mathbf{G}\left(\mathbf{U}^*_D\right)$. Between the states $\mathbf{U}_{RU}$ and $\mathbf{U}_{RD}$, we have the formation of a one-dimensional Riemann problem in the y-direction with a resolved state $\mathbf{U}^*_R$, as shown in Fig. 1b, and given explicitly by

$$\mathbf{U}^*_R = \frac{1}{2}\left(\mathbf{U}_{RU} + \mathbf{U}_{RD}\right) - \frac{1}{2S_U}\left(\mathbf{G}\left(\mathbf{U}_{RU}\right) - \mathbf{G}\left(\mathbf{U}_{RD}\right)\right) \tag{6.3}$$

From the state $\mathbf{U}^*_R$ we can also obtain the x-flux $\mathbf{F}\left(\mathbf{U}^*_R\right)$. Between the states $\mathbf{U}_{LU}$ and $\mathbf{U}_{LD}$, we have the formation of a one-dimensional Riemann problem in the y-direction with a resolved state $\mathbf{U}^*_L$, as shown in Fig. 1b. To obtain $\mathbf{U}^*_L$, just replace $R \to L$ in (6.3). From the state $\mathbf{U}^*_L$ we can also obtain the x-flux $\mathbf{F}\left(\mathbf{U}^*_L\right)$.

The four resolved states then interact to produce the strongly interacting state $\mathbf{U}^{**}$ which covers the z-edge, as shown in Fig. 1b. This is the state that will give us the z-edge-centered D^{**}_z and B^{**}_z that we seek. The method for obtaining this state is given in (13) of Balsara [7] and is explicitly written

$$\mathbf{U}^{**} = -\frac{1}{4S_R}\left[\mathbf{F}\left(\mathbf{U}^*_R\right) - S_R\mathbf{U}^*_R\right] + \frac{1}{4S_R}\left[\mathbf{F}\left(\mathbf{U}^*_L\right) + S_R\mathbf{U}^*_L\right]$$
$$-\frac{1}{4S_U}\left[\mathbf{G}\left(\mathbf{U}^*_U\right) - S_U\mathbf{U}^*_U\right] + \frac{1}{4S_U}\left[\mathbf{G}\left(\mathbf{U}^*_D\right) + S_U\mathbf{U}^*_D\right] \tag{6.4}$$

Once $\mathbf{U}^{**}$ is obtained, its third and sixth components give us the resolved z-edge-centered D^{**}_z and B^{**}_z that we seek. Once a multidimensional Riemann solver is developed as documented here, a cyclic rotation of its input variables can be used to yield multidimensional Riemann solvers that act in the yz-plane and xz-plane. This gives us all the edge-centered variables that are required for making a one-step update of (A.1) to (A.18) in the corrector step.

1a)

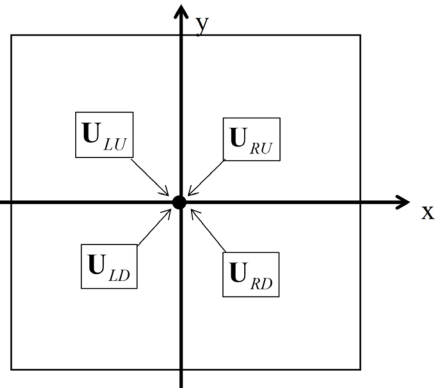

Fig. 1a shows four zones in the xy-plane that come together at the z-edge of a three-dimensional mesh. Since the mesh is viewed from the top in plan view, the z-edge is shown by the black dot and the four abutting zones are shown as four squares. The four states have subscripts given by "RU" for right-upper; "LU" for left-upper; "LD" for left-down and "RD" for right-down. Fig 1a shows the situation before the states start interacting via four one-dimensional and one multidimensional Riemann problems. The arrows indicate that higher-order space-time reconstruction within each of the four zones is used to obtain the four input states at the z-edge.

1b)

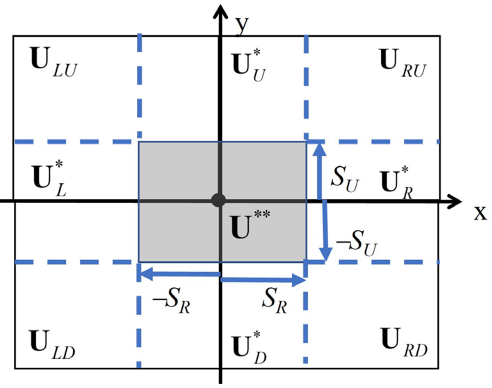

Fig. 1b shows the same situation as Fig. 1a. However, it shows the situation after the four incoming states from Fig. 1a start interacting with each other. Four one-dimensional Riemann problems, shown by dashed lines and single-starred states, develop between the four pairs of states. The shaded region with the double-starred state depicts the strongly interacting state that arises when the four one-dimensional Riemann problems interact with one another. We want to find the z-components of the electric displacement and magnetic induction in the strongly interacting state.

The two-dimensional Riemann solver presented here is such that it reduces precisely to a one-dimensional Riemann solver when all the variations are strictly in one dimension. For this reason, it is also suitable for use in two dimensional applications where all the variations in the third dimension are suppressed. This completes our description of the two-dimensional Riemann solver.

B. Description of the Single Stage Corrector Step

It is also valuable to describe a single stage update from time t^n to time $t^n + \Delta t$ for a mesh with zones of size Δx and Δy in the x- and y-directions. We instantiate that using (2.15), (2.16) and (2.17). Evaluated at any x-face, the update equation for D_x can be written as follows

$$D_x^{n+1} = D_x^n + \frac{\Delta t}{\langle \kappa_y \rangle \Delta y}\left(\langle B_z/\mu \rangle\big|_{y=\Delta y/2} - \langle B_z/\mu \rangle\big|_{y=-\Delta y/2} \right)$$

$$-\frac{\Delta t}{\langle \kappa_z \rangle \Delta z}\left(\langle B_y/\mu \rangle\big|_{z=\Delta z/2} - \langle B_y/\mu \rangle\big|_{z=-\Delta z/2} \right) + \Delta t\left(\langle Q^H_{y,z} \rangle - \langle Q^H_{z,y} \rangle \right)$$

(6.8)

In the above equation, $\langle \kappa_y \rangle$, $\langle \kappa_z \rangle$ are averaged over the area of the x-face being considered. The y-edge centered update terms $\langle B_y/\mu \rangle\big|_{z=\Delta z/2}$ and $\langle B_y/\mu \rangle\big|_{z=-\Delta z/2}$ are obtained from one space and one time integration over the upper and lower y-edges of the x-face being considered. The y-edge centered update terms $\langle B_z/\mu \rangle\big|_{y=\Delta y/2}$ and $\langle B_z/\mu \rangle\big|_{y=-\Delta y/2}$ are obtained from one space and one time integration over the upper and lower z-edges of the x-face being considered. The source terms $\langle Q^H_{y,z} \rangle$ and $\langle Q^H_{z,y} \rangle$ are obtained by two space and one time integration over the facial area from the two zones that abut the x-face being considered. The use of quadrature formulae in the corrector step, and the fact that the predictor and reconstruction steps taken together have produced space-time accurate inputs for the Riemann solver, ensures that the formulation of the corrector step extends naturally to all orders of accuracy. Now that the notation is established, it is easy to write the update equations for the further PML variables that reside in the x-face as follows

$$Q^{H;n+1}_{y,z} = Q^{H;n}_{y,z} - \frac{\Delta t}{\varepsilon_0 \Delta y}\left\langle \frac{\sigma_y}{\kappa_y^2} \right\rangle \left(\langle B_z/\mu \rangle\big|_{y=\Delta y/2} - \langle B_z/\mu \rangle\big|_{y=-\Delta y/2} \right)$$

$$-\frac{\Delta t}{\varepsilon_0}\left\langle \left(a_y + \left(\sigma_y/\kappa_y \right) \right) Q^H_{y,z} \right\rangle$$

(6.9)

and

$$Q^{H;n+1}_{z,y} = Q^{H;n}_{z,y} - \frac{\Delta t}{\varepsilon_0 \Delta z}\left\langle \frac{\sigma_z}{\kappa_z^2} \right\rangle \left(\langle B_y/\mu \rangle\big|_{z=\Delta z/2} - \langle B_y/\mu \rangle\big|_{z=-\Delta z/2} \right)$$

$$-\frac{\Delta t}{\varepsilon_0}\left\langle \left(a_z + \left(\sigma_z/\kappa_z \right) \right) Q^H_{z,y} \right\rangle$$

(6.10)

This completes our description of the single stage update step. Now that we have seen it for the x-faces, it is easy to extend it to all the other faces of the mesh.

VII. Pointwise Description of the Implementation of the PML Algorithm for FVTD

The implementation is based on three major algorithmic pieces, which are in some sense pivotal to the success of any higher order Godunov methodology. Conceptually, any one-step higher order Godunov scheme consists of the following three ingredients: 1) A higher order reconstruction step

(Sections III and IV), 2) A predictor step (Section V) and 3) A corrector step (Section VI). The first algorithmic piece consists of the reconstruction of all the relevant variables with sufficiently high order of spatial accuracy. The second algorithmic piece consists of making an "in-the-small" time evolution of the solution within each zone. This should be done with sufficiently good temporal accuracy and a fully implicit treatment of the stiff source terms. The third algorithmic piece consists of coupling the zones so that waves can flow across zones. This is done with the help of the multidimensional Riemann solver. The algorithm can be described in pointwise fashion as follows:-

1) Using the divergence constraint-preserving reconstruction algorithm from Section III, reconstruct the facial electric and magnetic flux densities. This provides us with the spatially reconstructed solution for the two vector fields that hold over the entire zone for all the zones of the mesh.

2) In just the zones where the PML is to be activated, use the WENO-ADP algorithm from Section IV to reconstruct the PML variables so that they are available over the entire zone of interest. This step only needs to be invoked in the PML-active zones.

3) Using the Implicit Taylor algorithm from Section V, obtain a space-time accurate representation of the solution at all the temporal quadrature points within each zone. This means that all the modes for all the variables that were reconstructed in steps 1) and 2) above are now available with sufficient space-time accuracy at all the temporal quadrature points within each zone.

4) Usually in CED, the material properties do not change in time, with the result that the matrices in (5.1) are not time-dependent. This ensures that it is acceptable to use time-integration at each of the spatial quadrature points within each face or edge where the 1D or 2D Riemann solvers will be applied. This is explained further in the last three Sub-sections of Section V.

5) The ADER step also produces all the source terms (i.e. the terms on the right hand sides) that will be needed a couple of steps later in the single stage update of (A.1) to (A.18). These source terms are fully time-implicit because of the Implicit Taylor ADER step. When the source terms are needed at any face, they can be obtained by averaging from the space-time evolved variables from the two zones that abut that face.

6) Using the time-integrated variables from either side of each face, apply the 1D Riemann solvers to obtain the desired face-centered variables. Similarly, using the time-integrated variables from the four zones that come together at each edge, apply the 2D Riemann solver to obtain the desired edge-centered variables. The outputs from the Riemann solvers will be spatially and temporally accurate. The Riemann solvers are described in Section VI. (In truly 3D calculations, only the multidimensional Riemann solvers need to be invoked at the edges of the mesh. The one-dimensional Riemann solvers are only needed when we have a 2D calculation.)

7) With those face-centered source terms in hand from Step 5, and edge-centered variables in hand from Step 6, carry out a single step update of the CED variables and the PML variables. This is the corrector step. It advances the solution from a time t^n to a time $t^n + \Delta t$ by making a single stage update of (A.1) to (A.18).

Notice that the parts of the mesh that rely on CED and the parts of the mesh where PML is invoked have exactly the same update algorithm with the exception of step 2) above. This makes it very easy to integrate our PML formulation in a pre-existing CED code. The third order reconstruction costs about twice as much as the second order reconstruction. The fourth order reconstruction costs about 2.5 times as much as the third order reconstruction. Similar ratios prevail with respect to the implicit Taylor ADER method. But please recall that in this method the reconstruction has to be done only once, and likewise for the ADER step. In other methods that use higher order Runge-Kutta updates in time, we remind the reader that the fourth order SSP-RK method requires five stages. In other words, there are considerable savings in the methods presented here. While we have not made a parallel implementation, a higher order Runge-Kutta method would also require multiple messaging steps, whereas this method only requires one messaging step per timestep.

VIII. AN OPTIMIZATION EXERCISE FOR PML

A. The Model Problem

In order to evaluate the performance of the PML, the numerical experiment presented in Taflove and Hagness ([41]) is performed (in Section 7.11.1). For this experiment, a TEz grid is used as shown in Fig. 2. The source is located in free space at the center of a 40 mm × 40 mm grid (at Point O in Fig. 2).

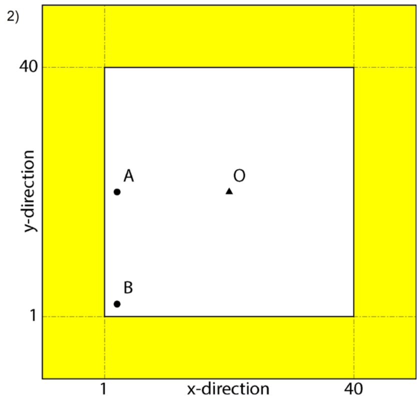

Fig. 2 - The experimental setup is shown. A y-directed electric current source is located at the center of the grid (point O) and the E-fields are recorded at points A and B. The main grid (in white) is surrounded by PML (in yellow).

The source is on a y-directed electric field and is set to a differentiated Gaussian pulse waveform defined as

$$J(t) = -2\left[\left(t-t_0\right)/t_w\right]\exp\left\{-\left[\left(t-t_0\right)/t_w\right]^2\right\} \tag{8.1}$$

where $t_w =$ $t_0 = 4t_w$. The grid has a resolution of 1 mm in both Cartesian directions and is surrounded by PML on all four sides (shown as the yellow region in Fig. 2).

PML thicknesses of 6 and 10 cells are tested. The simulation is run with a Courant-Friedrichs-Lewy (CFL) value of 0.4, to a final time of 3×10^{-9} seconds. A von Neumann analysis in Balsara and Kappeli [13] has shown that the FVTD schemes have a limiting CFL of 0.5. As a result, our choice of a CFL of 0.4 is quite large for this class of scheme.

Electric fields are recorded at observation points A and B in the grid. Point A is in the same y-plane as the source, but 2 mm away from the PML, and point B is 2 mm away from both the bottom and left sides of the PML. The observed electric fields at Points A and B are compared with the corresponding electric fields from a much larger grid (a reference grid) in which there are no reflections from the boundaries during the timespan of the simulation. The relative error, $\text{Rel.error}\big|_{i,j}^{n}$,caused by the PML at time step n and grid location (i,j) is calculated as

$$\text{Rel.error}\big|_{i,j}^{n} = \left| E\big|_{i,j}^{n} - E_{\text{ref}}\big|_{i,j}^{n} \right| \Big/ \left| E_{\text{ref},\max}\big|_{i,j}^{n} \right| \qquad (8.2)$$

where $E\big|_{i,j}^{n}$ is the electric field recorded at time step n and location (i,j), $E_{\text{ref}}\big|_{i,j}^{n}$ is the reference grid electric field recorded at time step n and at location (i,j), and $E_{\text{ref},\max}\big|_{i,j}^{n}$ is the maximum amplitude of the reference electric field at location (i,j) and over the entire time span of the simulation.

B. Optimization Exercise at Second Order for 10-cell and 6-cell PML

Similar to Taflove and Hagness [41], one has to undertake an optimization study to ensure that we get a PML with minimal back-reflection. We carry out such an optimization study independently for each order of accuracy because we have found that the optimal parameters change quite a bit as we go from second to third order. Fig. 3a shows the response of an optimized 10-cell PML for the model problem described in the previous Sub-section. The parameters used for this Figure are $(\sigma^{ref},\kappa^{\max},a^{\max},m)=(0.5,\ 25,\ 0.2,\ 3)$. Fig. 3a is optimized to minimize back-reflection at early times. We see that the early time response of our method is roughly comparable to FDTD; however the late time response is vastly superior. The late time response is very important because it shows us that any waves that may have interacted with matter on the computational domain will not back-reflect and build up error on the mesh. In that regard, observe that the waves do not damp out fast enough when FDTD is used. We attribute that to the fact that FVTD, via its use of the Implicit Taylor predictor step, treats the source terms in a fully implicit fashion, whereas FDTD is only half-implicit. This explains why FVTD at second order shows a vastly improved late-time response. It may even prove advantageous to optimize PML separately for its late-time response. This late time optimized performance can be achieved by using the parameters $(\sigma^{ref},\kappa^{\max},a^{\max},m)=(0.5,\ 25,\ 0.2,\ 4)$.

3a)

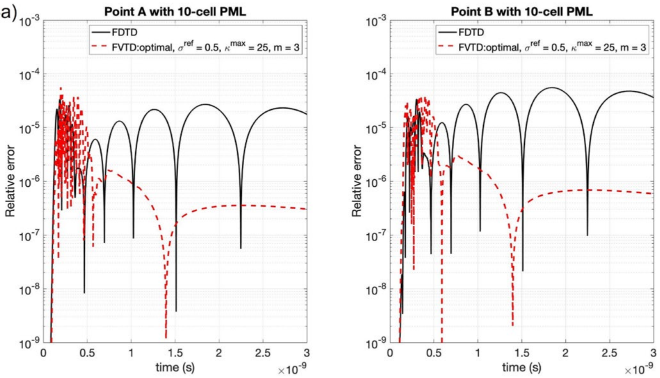

Fig 3a shows the optimal choice (early response) of 10-cell CPML for 2nd order FVTD. Relative error at points A (left panel) and B (right panel) for 10-cell CPML zones with the FDTD (black traces), 2nd order FVTD with the best performance at early and late times (red traces). Notice that in order to minimize reflection at late times we need quite large values of "s and k". Only the ADER formulation with Implicit Taylor gives this level of unconditional stability in the face of very large PML conductivities; thereby showing its unique utility for CED. Note too that the difference in early time behavior is only very slight between the optimized 2nd order FVTD and optimized FDTD. Also observe that the FDTD oscillations never die out at late times owing to its semi-implicit formulation; whereas at late times 2nd order FVTD is close to *two full orders of magnitude* better than FDTD!

Fig 3b shows the response of a 6-cell PML with $(\sigma^{ref},\kappa^{\max},a^{\max},m)=(0.5,\ 25,\ 0.2,\ 3)$. We see that it too performs very well and seems to outperform FDTD in early and late-time response. Notice too that if an optimization study is carried out with 10-cell PML, the use of the same parameters for 6-cell PML will usually yield an optimal 6-cell PML scheme. In other words, one can set optimal parameters for second order PML in a code and those parameters will work sufficiently well regardless of the number of cells in the PML. Fig. 4 shows how our optimal values for 2nd order accurate PML were obtained. The plot makes it quite easy to realize why Figs. 3a and 3b were indeed the optimal choices for PML at second order.

3b)

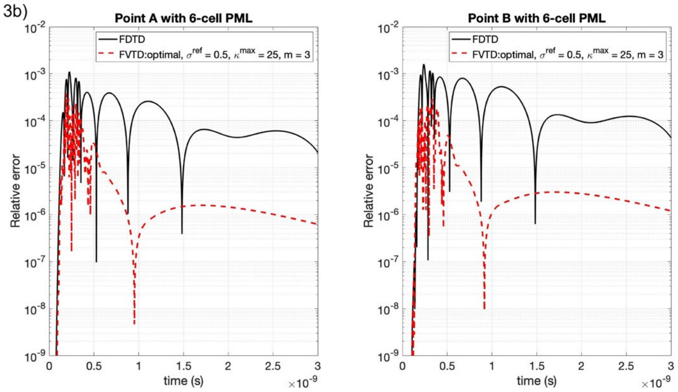

Fig 3b shows the optimal choice (early response) of 6-cell CPML for 2nd order FVTD. Relative error at points A (left panel) and B (right panel) for 6-cell CPML zones with the FDTD (black traces), 2nd order FVTD with the best performance at early and late times (red traces). Also observe that at late times 2nd order FVTD is close to *one and a half orders of magnitude* better than FDTD!

4)

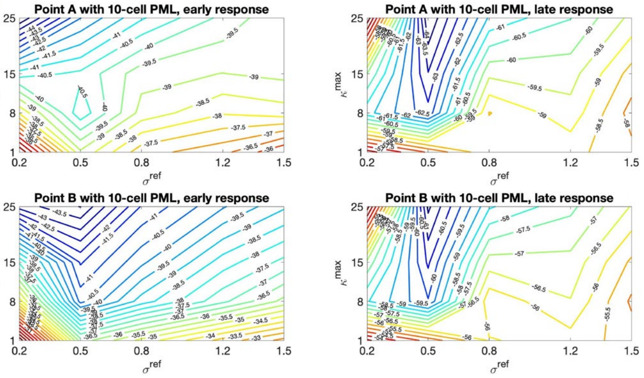

Fig 4. Decibel contour plots of the maximum relative error observed at points A (top row) and B (bottom row) as a function of σ^{ref} and κ^{max} for 10-cell CPMLs with the FVTD over early (left column) and late (right column) responses. The late responses only measure the error over times $[1.3,3]\times10^{-9}$. These plots allow us to choose optimal CPML parameters for 2nd order FVTD if we want to minimize the boundary response at early times or late times. Fortunately, the early and late response becomes optimal for the same parameter set that is centered at σ^{ref}=0.5 with increasing values of k. The previous figure shows that an optimized choice of CPML parameters can yield almost an order of magnitude improvement in the late time response.

C. Optimization Exercise at Third Order for 10-cell and 6-cell PML

Fig. 5a shows the response of an optimized 10-cell PML for the model problem. The parameters used for this Figure are $(\sigma^{ref},\kappa^{\max},a^{\max},m)=(0.3,\ 1.5,\ 0.2,\ 4)$. At early times, the third order PML with FVTD is marginally inferior to the FDTD, however please observe that at late times, our 3rd order FVTD scheme produces results that are three full magnitudes better than FDTD. Fig. 5b shows the response of an optimized 6-cell PML for the model problem. The parameters used for this Figure are still $(\sigma^{ref},\kappa^{\max},a^{\max},m)=(0.3,\ 1.5,\ 0.2,\ 4)$. We realize, therefore, that once a PML has been optimized for a certain layer width, it does not need to be optimized again when the layer width is altered. Fig. 6 shows how our optimal values for 3rd order accurate PML were obtained.

5a)

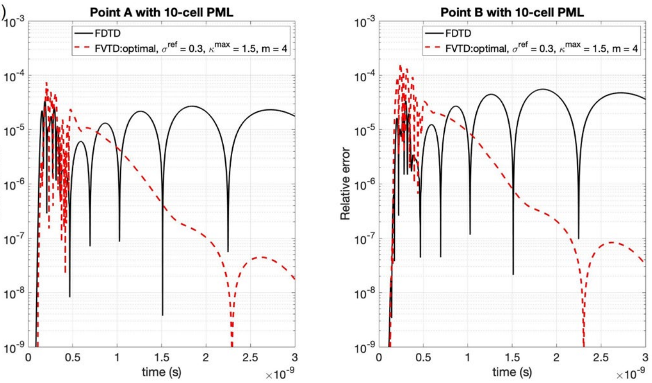

Fig 5a shows the optimal choice of 10-cell CPML for 3rd order FVTD. Relative error at points A (left panel) and B (right panel) for 10-cell CPML zones with the FDTD (black traces), 3rd order FVTD with the best performance at early and late times (red traces). Notice that in order to minimize reflection at late times we need quite small values of "s and k"; this is different from the 2nd order case. Note too that the difference in early time behavior is only very slight between the optimized 3rd order FVTD and optimized FDTD. The first few bounces at early time in Fig. 5 represent the first few reflections within the PML layer. They show a slightly larger value than FDTD because the higher order method also tries to simultaneously capture wave motion between the physical domain and the PEC at the outer boundary of the PML more accurately and with lower dispersion. In other words, the initial bounces represent a tussle between a method that wants to be more accurate in its wave propagation and a PML formulation that wants to damp waves. Also observe that the FDTD oscillations never die out at late times owing to its semi-implicit formulation; whereas at late times 3rd order FVTD is *three full orders of magnitude* better than FDTD!

5b)

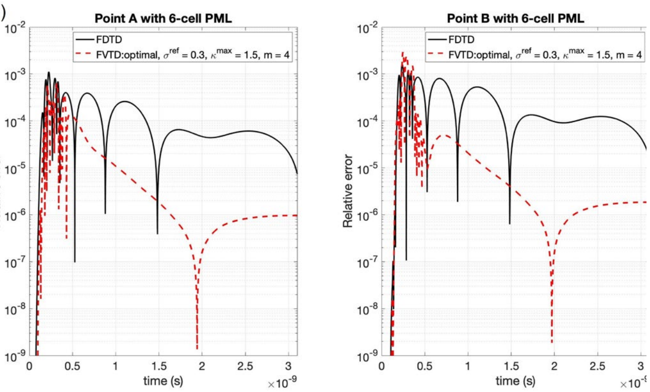

Fig 5b shows the optimal choice of 6-cell CPML for 3rd order FVTD. Relative error at points A (left panel) and B (right panel) for 6-cell CPML zones with the FDTD (black traces), 3rd order FVTD with the best performance at early and late times (red traces). Also observe that at late times 3rd order FVTD is *one full order of magnitude* better than FDTD!

6)

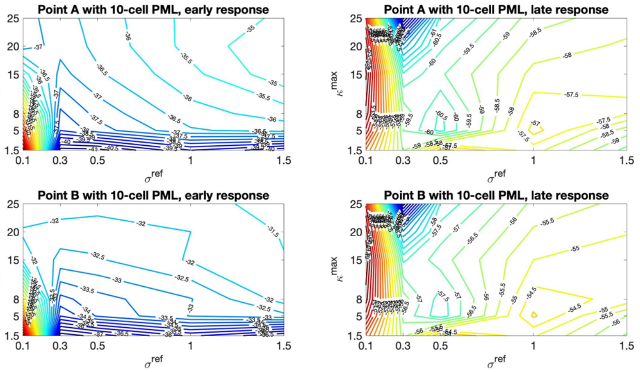

Fig 6. Decibel contour plots of the maximum relative error observed at points A (top row) and B (bottom row) as a function of σ^{ref} and κ^{max} for 10-cell CPMLs with the FVTD over early (left column) and late (right column) responses. The late responses only measure the error over times $[1.3,3]\times10^{-9}$. These plots allow us to choose optimal CPML parameters for 3rd order FVTD if we want to minimize the boundary response at early times or late times. Fortunately, the early and late response becomes optimal for the same parameter set that is centered at σ^{ref}=0.3 with somewhat lower values of k. The previous figure shows that an optimized choice of CPML parameters can yield almost two orders of magnitude improvement in the late time response.

D. Optimization Exercise at Fourth Order for 10-cell and 6-cell PML

Fig. 7a shows the response of an optimized 10-cell PML for the model problem. The parameters used for this Figure are $(\sigma^{ref},\kappa^{\max},a^{\max},m)=(0.3,\ 1.5,\ 0.2,\ 3)$

parameters used for this Figure are still $(\sigma^{ref}, \kappa^{\max}, a^{\max}, m) = (0.3,\ 1.5,\ 0.2,\ 3)$.

7a)

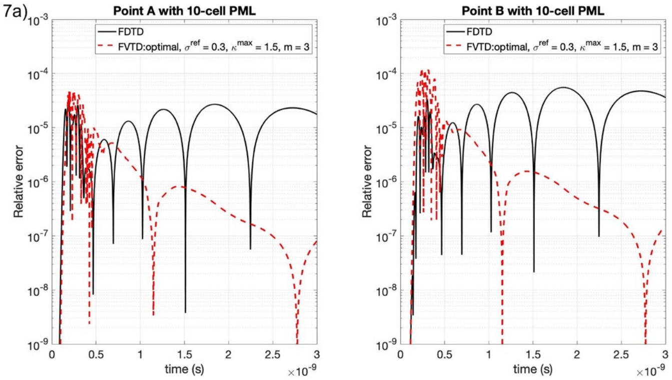

Fig 7a shows the optimal choice of 10-cell CPML for 4th order FVTD. Relative error at points A (left panel) and B (right panel) for 10-cell CPML zones with the FDTD (black traces), 4th order FVTD with the best performance at early and late times (red traces). Notice that in order to minimize reflection at late times we need quite small values of "s and k"; these are quite similar to the 3rd order case. Note too that the difference in early time behavior is only very slight between the optimized 4th order FVTD and optimized FDTD. The same explanation that applied to Fig. 5 for the early bounces also applies to Fig. 7. Also observe that the FDTD oscillations never die out at late times owing to its semi-implicit formulation; whereas at late times 4th order FVTD is *two and a half full orders of magnitude* better than FDTD!

7b)

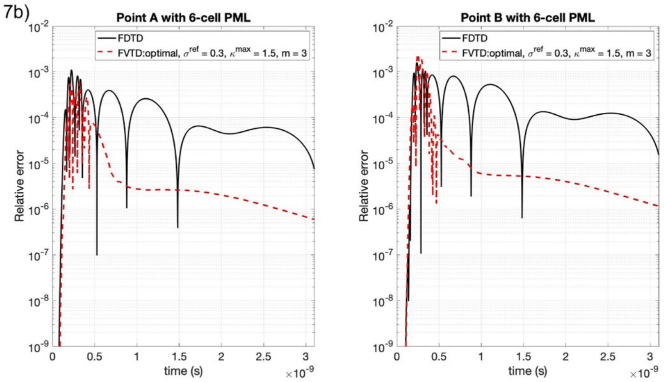

Fig 7b shows the optimal choice of 6-cell CPML for 4th order FVTD. Relative error at points A (left panel) and B (right panel) for 6-cell CPML zones with the FDTD (black traces), 4th order FVTD with the best performance at early and late times (red traces). Also observe that at late times 4th order FVTD is *one full order of magnitude* better than FDTD!

8)

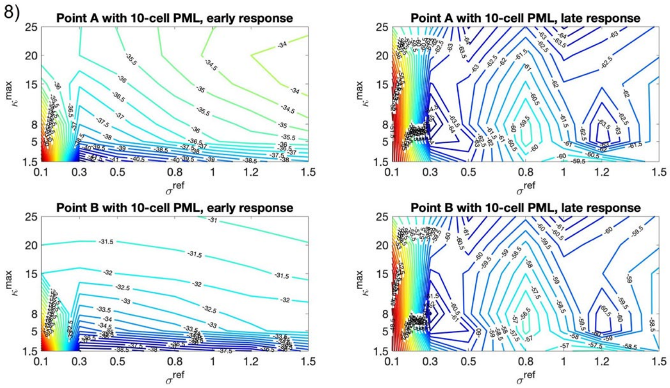

Fig 8. Decibel contour plots of the maximum relative error observed at points A (top row) and B (bottom row) as a function of σ^{ref} and κ^{max} for 10-cell CPMLs with the FVTD over early (left column) and late (right column) responses. The late responses only measure the error over times $[1.3,3]\times10^{-9}$. These plots allow us to choose optimal CPML parameters for 4th order FVTD if we want to minimize the boundary response at early times or late times. Fortunately, the early and late response becomes optimal for the same parameter set that is centered at σ^{ref}=0.3 with somewhat lower values of k. The previous figure shows that an optimized choice of CPML parameters can yield almost two orders of magnitude improvement in the late time response.

For the fourth order FVTD case also the realization that once a PML has been optimized for a certain layer width, it does not need to be optimized again when the layer width is altered stays consistent with the second and third order schemes. Fig. 8 shows how our optimal values for 4th order accurate PML were obtained.

IX. CONCLUSIONS

The emergence of high order accurate, globally divergence constraint-preserving FVTD schemes (Balsara *et al*. [9], [11], [12]) and DGTD schemes (Balsara and Käppeli [13], Hazra et al. [29], Balsara and Simpson [14]) calls for similarly accurate strategies for treating radiative boundaries. This is because in a CED calculation, the spuriously back-reflected waves interfere with the physical solution of the problem. Once such spurious waves are established on the computational domain, a higher order CED scheme will capture them and evolve them as if they are physical waves. For this extremely important reason, it is crucial to design superlative PML methods for the new classes of emerging FVTD and DGTD schemes. In this paper we focus on high order accurate, globally divergence constraint-preserving FVTD schemes for CED. A version of CPML is derived and presented in Section II and the Supplement A which is closely conformant with the structure of the FVTD scheme itself.

The electric and magnetic flux densities form the primal variables for our scheme. Innovations in the constraint-preserving reconstruction of electric and magnetic flux densities are described in Section III. The most beneficial collocation of CPML variables is also described. The corresponding reconstruction of the CPML variables can be carried out with the newly-invented WENO-ADP method of Balsara, Samantaray and Subramanian [15] and that method is described with more helpful details in Section IV. The Implicit Taylor ADER predictor step is another highly novel invention and it is described in Section V. It is important because it allows us to tackle the stiff CPML source terms in a fully time-implicit fashion at all orders of accuracy. The Implicit Taylor ADER formulation presented here is uniquely well-suited for CED calculations.

Section VI describes the 1D and 2D Riemann solvers and their role in the corrector step. Consequently, a full timestep consists of a reconstruction step that is high order accurate in space. This is followed by the Implicit Taylor ADER predictor step which gives us a suitably high order temporal extension of the reconstructed variables. The application of the Riemann solvers in the corrector step, and the use of the same to obtain a full space-time accurate update, then completes the method. Section VII describes implementation-related details in step-by-step fashion and an optimization study in Section VIII yields the desired results.

Based on this work we see that the CPML parameters should be optimized differently for each order of accuracy. However, once optimized, the same parameters perform optimally for both the 6-cell and 10-cell PML. Therefore, once an optimal set of parameters is packaged into a code for each different order of accuracy, it can be used for a range of PML layers. The optimal PML parameters for second, third and fourth order accurate FVTD schemes have been documented in this paper. We also find that the late time behavior of the CPML described here is several orders of magnitude better than the behavior of CPML in FDTD schemes. We attribute that to our use of the fully-implicit Taylor ADER methods developed here, which contrast quite starkly with the half-implicit methods that are traditionally used in FDTD. In a subsequent work we shall extend this PML formulation to globally divergence constraint-preserving DGTD schemes. Since our formulation is also fully general, we will also extend it to FDTD and DGTD schemes for polarized media in subsequent papers.

At the end of Section VII we have pointed out one advantage of this method as it pertains to parallelism. In Section V it can also be observed that this method makes optimal use of matrix multiplications, which is going to be a forte of the upcoming GPU architectures. In Balsara, Samantaray and Subramanian [15] we have also shown that the global constraint preservation in these methods is a big asset in overcoming the late time instability that is present in AMR calculations involving CED. We see, therefore, that the methods presented have their own strong suits.

CRediT Authorship Contribution Statement

DSB & SS -- writing most of the paper. KN & JJS -- writing Section II and small parts of Section VIII. KN, JJS & DSB -- formulation in Section II. DSB -- formulation and code implementation of Sections III, IV and VI. DSB, SS & GM -- formulation of Section V. DSB, SS and KN – code implementation of Section V. SS -- simulations in Section VIII. KN -- graphics for Section VIII.

ACKNOWLEDGMENT

The authors wish to acknowledge support from NSF-19-04774. DSB also wishes to acknowledge support from NSF-AST-2009776 and NASA-2020-1241.

REFERENCES

[1] L. D. Angulo, J. Alvarez, M. F. Pantoja, S. G. Garcia, and A. R. Bretones, *Discontinuous Galerkin Time Domain Methods in Computational Electrodynamics: State of the Art*, Forum for Electromagnetic Research Methods and Application Technologies (FERMAT).

[2] D.S. Balsara , *Divergence-free adaptive mesh refinement for magnetohydrodynamics*, Journal of Computational Physics 174 (2001) 614-648.

[3] D. S. Balsara, *Second-order-accurate schemes for magnetohydrodynamics with divergence-free reconstruction*, Astrophysical Journal Supplement 151 (2004) 149-184.

[4] D.S. Balsara, *Divergence-free reconstruction of magnetic fields and WENO schemes for magnetohydrodynamics*, J. Comput. Phys., 228 (2009) 5040-5056.

[5] D.S.Balsara, *Multidimensional HLLE Riemann solver; Application to Euler and Magnetohydrodynamic Flows*, J. Comput. Phys., 229 (2010) 1970-1993.

[6] D.S. Balsara, *A two-dimensional HLLC Riemann solver for conservation laws: Application to Euler and magnetohydrodynamic flows*, Journal of Computational Physics 231 (2012) 7476-7503.

[7] D.S. Balsara, *Multidimensional Riemann Problem with Self-Similar Internal Structure – Part I – Application to Hyperbolic Conservation Laws on Structured Meshes*, Journal of Computational Physics 277 (2014) 163-200.

[8]D.S. Balsara, S. Garain, and C.-W. Shu, *An efficient class of WENO schemes with adaptive order,* Journal of Computational Physics, 326 (2016c) 780-804.

[9]D. S. Balsara, T. Amano, S. Garain, J. Kim, *High Order Accuracy Divergence-Free Scheme for the Electrodynamics of Relativistic Plasmas with Multidimensional Riemann Solvers*, Journal of Computational Physics, vol. 318, pp. 169-200, 2016.

[10] D. S. Balsara and B. Nkonga, *Formulating Multidimensional Riemann Solvers in Similarity Variables – Part III :A Multidimensional Analogue of the HLLI Riemann Solver for Conservative Hyperbolic Systems*, Journal of Computational Physics, vol. 346, pp. 25-48, 2017.

[11] D. S. Balsara, A. Taflove, S. Garain and G. Montecinos, *Computational Electrodynamics in Material Media with Constraint-Preservation, Multidimensional Riemann Solvers and Sub-Cell Resolution – Part I, Second-Order FVTD Schemes*, Journal of Computational Physics, vol. 349, pp. 604-635, 2017.

[12] D. S. Balsara, A. Taflove, S. Garain and G. Montecinos, *Computational Electrodynamics in Material Media with Constraint-Preservation, Multidimensional Riemann Solvers and Sub-Cell Resolution – Part II, Higher-Order FVTD Schemes*, Journal of Computational Physics, vol. 354, pp. 613-645, 2018.

[13] D. S. Balsara and R. Käppeli, *von Neumann Stability Analysis of Globally Constraint-Preserving DGTD and PNPM Schemes for the Maxwell Equations using Multidimensional Riemann Solvers*, Journal of Computational Physics, no. 376, pp. 1108-1137, 2019.

[14] D. S. Balsara, J. J. Simpson, *Making a Synthesis of FDTD and DGTD Schemes for Computational Electromagnetics*, IEEE Journal on Multiscale and Multiphysics Computational Techniques, 2020, 5, pp. 99–118, 9115845.

[15] D.S. Balsara S. Samantaray and S. Subramanian, *Efficient WENO-Based Prolongation Strategies for Divergence-Preserving Vector Fields*, submitted Communications in Applied Mathematics and Computation, (2021)

[16] A. Barbas and P. Velarde, *Development of a Godunov method for Maxwell's equations with Adaptive Mesh Refinement*, Journal of Computational Physics, 300 (2016) 186-201.

[17] Chen, Liang, Mehmet Burak Özakın, Shehab Ahmed, and Hakan Bagci. "A Memory-Efficient Implementation of Perfectly Matched Layer With Smoothly Varying Coefficients in Discontinuous Galerkin Time-Domain Method." IEEE Transactions on Antennas and Propagation 69, no. 6 (2020): 3605-3610.

[18] Chew, W. C., and J. M. Jin. "Perfectly matched layers in the discretized space: An analysis and optimization." Electromagnetics 16, no. 4 (1996): 325-340.

[19] Cockburn, B., and Shu, C.-W., *The Runge-Kutta discontinuous Galerkin method for Conservation Laws V: Multidimensional systems*, Journal of Computational Physics, vol. 141, pp. 199-224, 1998.

[20] Cockburn, B., and Shu, C.-W., *Runge-Kutta Discontinuous Galerkin methods for convection dominated problems,* Journal of Scientific Computing, vol. 16, pp. 173-261, 2001.

[21] B. Cockburn, F. Li and C.-W. Shu, *Locally discontinuous Galerkin methods for the Maxwell equations*, Journal of Computational Physics, vol. 194, pp. 588-610, 2004.

[22] J.-P. Berenger, *A perfectly matched layer for the absorption of electromagnetic waves*, J. Comput. Phys. 114(2) (1994) 185–200.

[23] J.-P. Berenger, *Three-dimensional perfectly matched layer for the absorption of electromagnetic waves*, J. Comput. Phys. 127(2) (1996) 363–379.

[24] S. D. Gedney, *An anisotropic perfectly matched layer-absorbing medium for the truncation of FDTD lattices*, IEEE Transactions on Antennas and Propagation, vol. 44, no. 12, pp. 1630-1639, 1996.

[25] S. D. Gedney, *Perfectly Matched Layer Absorbing Boundary Conditions, in Computational Electrodynamics: The Finite-Difference Time-Domain Method*, 3rd ed., Artech House, Inc., pp. 273-328, 2005.

[26] Gedney, Stephen D., Chong Luo, J. Alan Roden, Robert D. Crawford, Bryan Guernsey, Jeffrey A. Miller, Tyler Kramer, and Eric W. Lucas. "The discontinuous Galerkin finite-element time-domain method solution of

Maxwell's equations." ACES Journal-Applied Computational Electromagnetics Society 24, no. 2 (2009): 129.

[27] S. D. Gedney, and B. Zhao, *An Auxiliary Differential Equation Formulation for the Complex-Frequency Shifted PML*, IEEE Transactions on Antennas and Propagation, vol. 58, pp. 838-847, 2010. https://doi.org/10.1109/TAP.2009.2037765.

[28] S. D. Gedney, *The Perfectly Matched Layer (PML) Absorbing Medium, in Introduction to the Finite-DifferenceTime-Domain (FDTD) Method for Electromagnetics*, C. A. Balanis, Ed., Morgan & Claypool, 2011, pp. 113-135.

[29] A. Hazra, P. Chandrashekar, and D.S. Balsara, *Globally constraint-preserving FR/DG scheme for Maxwell's equations at all orders*, accepted, Journal of Computational Physics, 2019.

[30] Hesthaven, Jan S., and Tim Warburton. "Nodal high-order methods on unstructured grids: I. Time-domain solution of Maxwell's equations." Journal of Computational Physics 181, no. 1 (2002): 186-221.

[31] T.Z. Ismagilov, *Second order finite volume scheme for Maxwell's equations with discontinuous electromagnetic properties on unstructured meshes*, Journal of Computational Physics, 282 (2015) 33–42.

[32] D.S. Katz, E.T. Thiel and A. Taflove, *Validation and extension to three dimensions of the Berenger PML absorbing boundary condition for FD-TD meshes*, IEEE Microwave and Guided Wave Letters, 4(8) (1994) 268.

[33] Gino I. Montecinos, Eleuterio F. Toro, *Reformulations for general advection-diffusion-reaction equations and locally implicit ADER schemes*. J. Comput. Phys. 275 (2014), 415–442.

[34] Gino I. Montecinos, Dinshaw S. Balsara, *A simplified Cauchy-Kowalewskaya procedure for the local implicit solution of generalized Riemann problems of hyperbolic balance laws. Comput. & Fluids* 202 (2020), 104490, 16 pp.

[35] Gino I. Montecinos, *Universal scheme; Generalized Riemann problems; hyperbolic balance laws; ADER schemes*, to appear, Journal of Computational Physics, 2021.

[36] Lu, Tiao, Pingwen Zhang, and Wei Cai. "Discontinuous Galerkin methods for dispersive and lossy Maxwell's equations and PML boundary conditions." Journal of Computational Physics 200, no. 2 (2004): 549-580.

[37] C.-D. Munz, P. Omnes, R. Schneider, E. Sonnendrücker, and U. Voß, *Divergence correction techniques for Maxwell solvers based on a hyperbolic model*, Journal of Computational Physics, 161 (2000) 484.

[38] J. A. Roden and S. D. Gedney, *Convolution PML (CPML): An efficient FDTD implementation of the CFS–PML for arbitrary media*, Microwave and Optical Technology Letters, vol. 27, no. 5, pp. 334-339, 2000.

[39] Q. Ren, Q. Sun, L. Tobón, Q. Zhan, and Q.H. Liu, *EB Scheme-Based Hybrid SE-FE DGTD Method for Multiscale EM Simulations*, IEEE Transactions on Antennas and Propagation, vol. 64(9) pp. 4088-4091, 2017.

[40] Q. Sun, R. Zhang, Q. Zhan, and Q.H. Liu, *A Novel Coupling Algorithm for Perfectly Matched Layer With Wave Equation-Based Discontinuous Galerkin Time-Domain Method*, IEEE Transactions on Antennas and Propagation, vol. 66(1), pp. 255-261, 2018.

[41] A. Taflove and S. Hagness, *Computational Electrodynamics: The Finite-Difference Time-Domain Method*, 3rd edition, Artech House, 2005.

[42] A. Taflove, A. Oskooi and S. Johnson, *Advances in FDTD Computational Electrodynamics – Photonics and Nanotechnology*, Artech House (2013).

[43] A. Taflove and S. Hagness, *Finite Difference Time Domain Solution of Maxwell's Equations*, WEEEE Review (2016) 8303.

[44] Toro, Eleuterio F.; Montecinos, Gino I. *Implicit, semi-analytical solution of the generalized Riemann problem for stiff hyperbolic balance laws. J. Comput. Phys.* 303 (2015), 146–172.

[45] H. Wang, L. Xu, B. Li, S. Descombes, and S. Lantéri, *A New Family of Exponential-Based High-Order DGTD Methods for Modeling 3-D Transient Multiscale Electromagnetic Problems*, IEEE Transactions on Antennas and Propagation, vol. 65(11), pp. 5960-5974, 2017.

[46] K.S. Yee, *Numerical Solution of Initial Boundary Value Problems Involving Maxwell Equation in an Isotropic Media*, IEEE Trans. Antenna Propagation 14 (1966) 30